STATISTICAL ANALYSIS OF A THREE-DIMENSIONAL AXIAL STRAIN AND AXIAL-SHEAR STRAIN ELASTOGRAPHY ALGORITHM

A Thesis

by

MOHAN LI

Submitted to the Office of Graduate Studies of
Texas A&M University
in partial fulfillment of the requirements for the degree of

MASTER OF SCIENCE

August 2011

Major Subject: Electrical Engineering

Statistical Analysis of a Three-dimensional

Axial Strain and Axial-shear Strain

Elastography Algorithm

STATISTICAL ANALYSIS OF A THREE-DIMENSIONAL AXIAL STRAIN AND AXIAL-SHEAR STRAIN ELASTOGRAPHY ALGORITHM

A Thesis

by

MOHAN LI

Submitted to the Office of Graduate Studies of
Texas A&M University
in partial fulfillment of the requirements for the degree of

MASTER OF SCIENCE

Approved by:

Chair of Committee,	Raffaella Righetti
Committee Members,	Jim Ji
	Deepa Kundur
	Ann McNamara
Head of Department,	Costas Georghiades

August 2011

Major Subject: Electrical Engineering

ABSTRACT

Statistical Analysis of a Three-dimensional Axial Strain and
Axial-shear Strain Elastography Algorithm. (August 2011)
Mohan Li, B.S., University of Science and Technology of China
Chair of Advisory Committee: Dr. Raffaella Righetti

Pathological phenomena often change the mechanical properties of the tissue. Therefore, estimation of tissue mechanical properties can be of clinical importance. Ultrasound elastography is a well-established strain estimation technique. Until recently, mainly 1D elastography algorithms have been developed. A few 2D algorithms have also been developed in the past. Both of these two types of technique ignore the tissue motion in the elevational direction, which could be a significant source of decorrelation in the RF data. In this thesis, a 3D elastography algorithm that estimates all the three components of tissue displacement is implemented and tested statistically.

In this research, displacement fields of mechanical models are simulated. RF signals are then generated based on these displacement fields and used as the input of elastography algorithms. To evaluate the image quality of elastograms, absolute error, SNR_e, CNR_e and CNR_{asse} are computed. The SNR_e, CNR_e and CNR_{asse} values are investigated not only under different strain conditions, but also in different frame locations, which forms 3D strain filters. A statistical comparison between image qualities of the 3D technique and 2D technique is also provided.

The results of this study show that the 3D elastography algorithm outperforms the 2D elastography algorithm in terms of image quality and robustness, especially under high strain conditions. This is because the 3D algorithm estimates the elevational displacement, while the 2D technique only estimates the axial and lateral deformation. Since the elevational displacement could be an important source for the decorrelation in the RF data, the 3D technique is more effective and robust compared with the 2D technique.

ACKNOWLEDGEMENTS

I would like to thank my committee chair, Dr. Raffaella Righetti, for providing me constant support throughout my research. Her guidance and encouragement are indispensable for the accomplishment of this thesis. I also appreciate the help from my committee members: Dr. Jim Ji, Dr. Deepa Kundur and Dr. Ann McNamara. Their suggestions are valuable for me for improving my work.

I am glad to thank Anuj Chaudhry for providing me the software of 2D RF simulation. I am also grateful to Xu Yang for his suggestions on my research and presentation.

Finally, I would like to thank all my friends I have made in the United States. Without them, my life would be much more difficult.

NOMENCLATURE

CNR_{asse}	Axial-shear Strain Contrast-to-Noise Ratio
CNR_e	Elastographic Contrast-to-Noise Ratio
FEM	Finite Element Model
FFT	Fast Fourier Transform
MAE	Mean Absolute Error
NCC	Normalized Cross-Correlation
PSF	Point Spread Function
RF	Radio Frequency
ROI	Region of Interest
SNR_e	Elastographic Signal-to-Noise Ratio
SNR_s	Sonographic Signal-to-Noise Ratio
SSE	Staggered Strain Estimation
TDE	Time Delay Estimation
US	Ultrasound

TABLE OF CONTENTS

CHAPTER Page

LIST OF FIGURES

Page

Page

LIST OF TABLES

Page

CHAPTER I

INTRODUCTION

1.1 Introduction

Conventional ultrasound (US) detects tissue abnormalities by imaging the echogenicity of tissues. This is based on the fact that pathological phenomena may induce changes in the tissue acoustic backscatter properties. However, abnormal tissues may have echogenicity properties similar to the normal ones and thus invisible in standard ultrasound examination. Pathological processes often involve significant change in the tissue mechanical properties, such as the stiffness (Anderson and Kissane 1953, Lendon et al. 1991, Lee et al. 1991, Ariel and Cleary 1987). For example, many cancers are much harder than surrounding tissues and some diseases involve fatty or collagenous deposits increase or decrease tissue elasticity (Ophir et al. 1991). Therefore, estimation of tissue mechanical properties can be of clinical importance and complement conventional US methods.

US elastography is a well-established strain estimation technique (Ophir et al. 1991, 1996, 1997, 1999). Subjected to a given stress, soft tissue areas will have larger deformation than hard tissue areas. In elastography, an external compression is usually applied to the tissue under investigation and both pre- and post- compression radio-

---

This thesis follows the style of Ultrasound in Medicine and Biology.

frequency (RF) data are acquired. Elastography algorithms estimate tissue motion by comparing the two data sets. The gradient of the estimated displacement image yields the elastogram (strain estimate).

US elastography has been widely used in the investigation of stiff tumors in soft tissues, such as the breast cancers (Garra et al. 1997, Hall et al. 2002, Doyley et al. 2001) and prostate cancers (Hiltawsky et al. 2001, Lorenz et al. 1999). Other applications include monitoring HIFU lesions (Righetti et al. 1999), imaging the myocardium (Konofagou et al. 2002), studying renal pathology (Emelianov et al. 1995), monitoring thermal changes of the tissue (Varghese et al. 2002) and skin abscess diagnosis (Gaspari et al. 2009).

Until recently, one-dimensional (1D) algorithms have been primarily developed for elastography applications. In this algorithm, short segments of pre- and post-compression A-lines are compared. The A-lines are first segmented using windows, corresponding segments in the pre- and post- compression data are then correlated, and the local axial displacement for each window is estimated (Ophir et al. 1991, Alam et al. 1998, Brusseau et al. 2000). A few two-dimensional (2D) algorithms have also been developed in the past (Seferidis and Ghanbari 1994, Yeung et al. 1998, Basarab et al. 2008). Instead of windowing and comparing the 1D segments, in the 2D methods frame of RF data is divided into 2D blocks, and the tissue motion is estimated in two directions (axial and lateral).

Tissue deformation during external load is three-dimensional. When a tissue is compressed axially, axial, lateral and elevational (out-of-plane) tissue displacements are

generated. Moreover, when the US RF data are acquired freehand (preferred technique in clinical applications), it is difficult to control the compression, which may cause significant lateral and elevational motions (Deprez et al. 2008). Thus, several of the proposed 1D and 2D elastography techniques are inherently inaccurate. The 1D elastography techniques typically consider the axial deformation of the tissue only and ignore lateral and elevational motions. Left uncorrected, lateral and elevational motions can cause significant decorrelation between pre- and post- compression data and degrade the image quality of the resulting elastograms (Kallel and Ophir 1997). 2D elastography methods include the lateral displacement estimation, but do not account for the elevational motion. To achieve complete estimation of tissue motion, all the three components of the displacement should be imaged. It is expected that 3D elastography techniques might be more precise and robust than 1D and 2D techniques, especially in situations that involve large deformations. Additionally, 3D elastography algorithm may allow computing more components of the displacement and strain tensor and provide more information about the mechanical properties of the tissue, such as anisotropy, compressibility and poroelasticity (Konofagou et al. 2001).

To estimate 3D tissue motion, 3D elastography techniques require US RF volumes as input (Konofagou et al. 2000). Theoretically, properly combining multiple RF data planes can form such volumes. These planes can be acquired by moving a 1D linear array in elevational direction and collecting a series of RF frames step by step. Modern US systems also allow usage of motorized US transducer that can provide RF volume data directly. Alternatively, the development of 2D transducer arrays enables the

acquisition of 3D RF data sets, thus facilitating the application of 3D elastography methods.

A few 3D elastography algorithms have been developed to date. For some of these techniques (Deprez et al. 2008, 2009), 3D volumes are selected from the pre- and post-compression RF data sets and optimization of 3D correlation coefficient function is performed to estimate the axial scaling factor, the lateral shift and the elevational shift. An alternative method is based on the complex cross-correlation (CCC) (Lindop et al. 2006). The CCC of a pair of complex time-shifted signals has zero phase at the displacement where the signals match. Gradient descent algorithm can be applied to find the phase zero, which yields accurate and fast motion estimation.

1.2 Research Plan

In this thesis, I have developed a 3D elastography block-matching algorithm. I also analyzed the statistical performance of this algorithm using a 3D simulation tool. More specifically, the research developed in this thesis consists of the following components:

1. Development of a 3D elastography algorithm that provides: 3D displacements and 3D axial strain and axial-shear strain elastograms;
2. Generation of a 3D US simulation software to test the performance of the developed elastography algorithm;

3. Statistical analysis of the performance of the algorithm in terms of accuracy, elastographic signal-to-noise ratio (SNR_e), elastographic contrast-to-noise ratio (CNR_e) and axial-shear strain contrast-to-signal ratio (CNR_{asse}), and statistical comparison with the performance of a 2D algorithm.

The 3D elastography algorithm developed in this work is based on a 3D volume-matching technique previously proposed. It selects one small volume of RF data from the pre-compression RF data and selects a larger volume from the post-compression RF data. The centers of these two volumes have the same location in the 3D RF data sets. It then estimates the time delay by computing the normalized cross-correlation (NCC) function between the two volumes and finding out the best match. A global stretching is applied prior to the volume-matching to increase the correlation between pre- and post-compression volume data. After the displacement volumes are obtained, a staggered strain estimator is used to compute the local strains (Srinivasan et al. 2002b). In this thesis, I considered only axial strain and axial-shear strain estimated using the 3D elastography algorithm.

The simulation used to evaluate the performance of the proposed 3D algorithm consists of three steps: generation of the mechanical model; RF simulation and generation of the simulated elastograms using the 3D elastography software (see Figure 1.1).

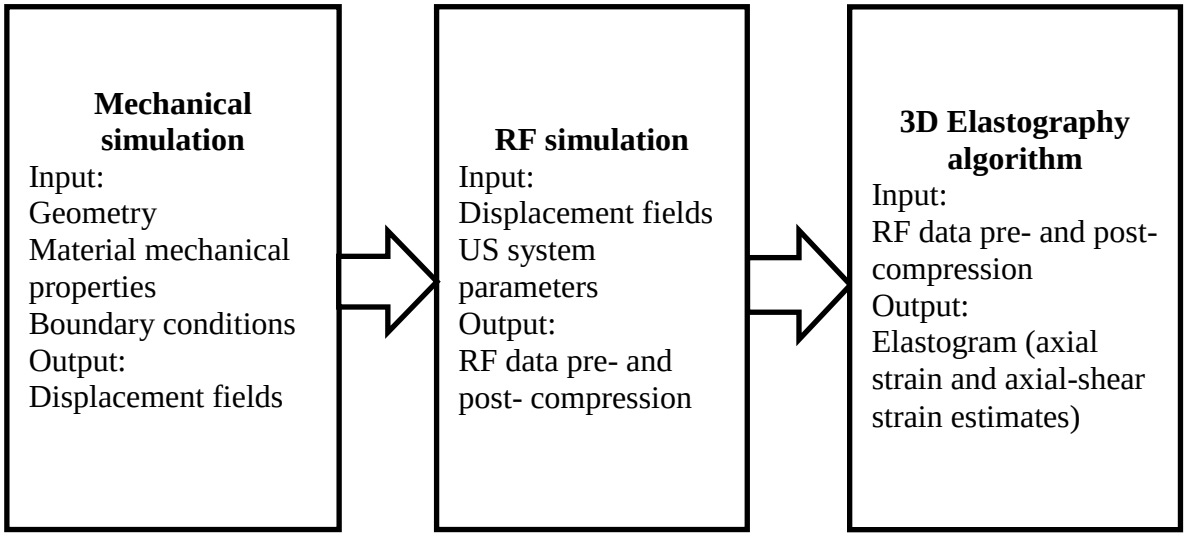

Figure 1.1 Simulation model used in this thesis

For the mechanical simulation, a commercially available finite element model (FEM) software package (COMSOL Multiphysics) is used in this thesis. Given the information of model geometry, mechanical properties and boundary conditions, the software yields the three components of the ideal displacement field.

3D RF simulation was then implemented as an extension of our in-house 2D RF simulation software (Chaudhry 2010). The basic ideal of this RF simulation is based on the convolution theory: the echo signal can be represented as the convolution of the US system point spread function (PSF) and the tissue scattering function. The PSF is modeled as a product of three components: a Gaussian modulated cosine pulse in the axial direction and two Gaussian functions in the lateral and elevational directions. The scattering amplitude of the tissue is modeled as independent and identically distributed Gaussian random variables in a 3D space. The output of the RF simulator is a set of

simulated pre- and post- compression RF frames equidistantly spaced in the elevational direction.

1.3 Structure of Thesis

This thesis is organized as follow. Chapter II describes the simulation methods used to generate the ideal displacement fields and RF signals. Chapter III provides the technical details of the 3D elastography algorithm developed in this thesis. Chapter IV explains methods and results of the image quality analysis of the 3D elastography algorithm (including the concept of 3D strain filters (Varghese and Ophir 1997)). Chapter V discusses the results of statistical analysis performed to evaluate the image quality of the 3D elastography algorithm. Conclusions and future work are included in Chapter VI.

CHAPTER II

SIMULATION MODEL

2.1 Mechanical Simulation

In this thesis I used a finite element method (FEM) based software package (COMSOL Multiphysics) to simulate the 3D displacement field in the media. Given the geometry of the model, material properties and boundary conditions, the FEM software yields the 3D scatterer motion under external compression with high accuracy. The results generated by the FEM software can be extracted using MATLAB and then utilized for statistical analysis.

To study the performance of 3D elastography algorithms, two mechanical models were simulated. A uniform cube phantom (Figure 2.1) was generated for SNR_e study and a cube phantom containing a spherical inclusion (Figure 2.2) was generated for CNR_e and CNR_{asse} studies. It should be noted that spherical inclusion models are often used in elastography study because they can be used to simulate tumors and other tissue lesions (Patil et al. 2008, Deprez et al. 2009). Technical details of these two models are listed in Table 2.1 and Table 2.2, respectively. The x axis, y axis and z axis in the model correspond to elevational, lateral and axial directions, respectively.

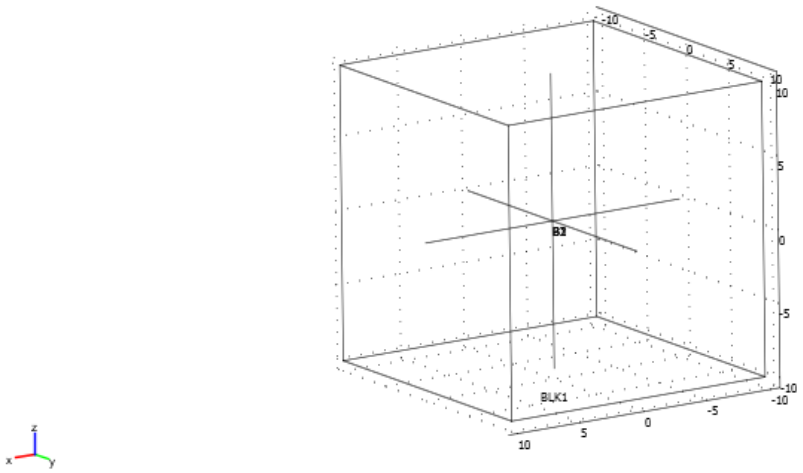

Figure 2.1 Geometry of the uniform simulation model

Table 2.1 Specification of the uniform simulation model

Size of cube	$20 \times 20 \times 20\ mm^3$
Number of nodes	17353
Shape of nodes	triangular
Young's modulus	$1\ kPa$
Poisson's ratio	0.495
Applied Strain values	0.2% ~ 15%

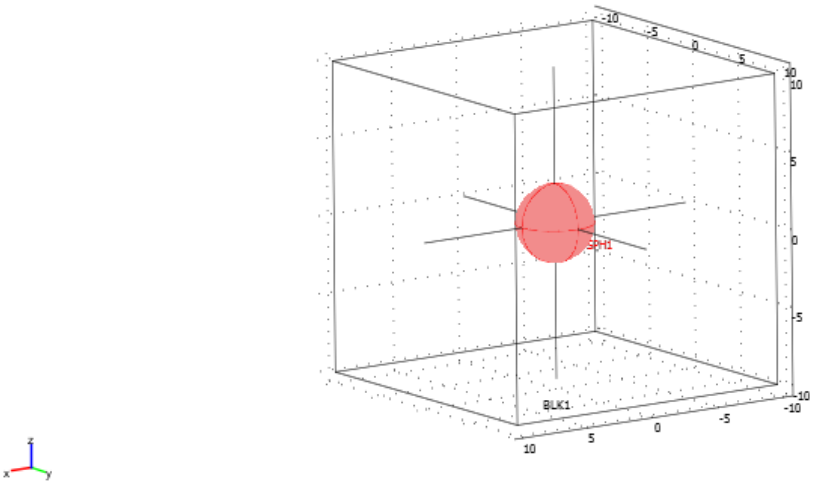

Figure 2.2 Geometry of simulation model with spherical inclusion

Table 2.2 Specification of simulation model with spherical inclusion

Size of cube	$20 \times 20 \times 20\ mm^3$
Number of nodes	18118
Shape of nodes	triangular
Young's modulus of background	$1\ kPa$
Poisson's ratio of background	0.495
Radius of inclusion	$2.5\ mm$
Young's modulus of inclusion	$3\ kPa$ or $10\ kPa$
Poisson's ratio of inclusion	0.495
Applied strain values	0.08% ~ 8%

The external compression was applied by prescribing the displacement of the upper surface of the cube phantom. For example, if the strain was 1%, then the displacement of the upper surface would be set as -0.2 mm along z axis (the minus means the displacement is downwards) and zero in other two directions. The bottom surface of the cube phantom always had no motion along the z axis. No constraint was imposed on the four vertical surfaces.

Though theoretically the model geometry, material mechanical properties and boundary conditions are sufficient to determine the displacement field in the phantom, the COMSOL may yield incorrect results when only these three parameters are provided. This might be due to the instability of differential equations solved by the FEM software. One way to overcome this problem is to provide more constraints inside the simulated medium. Therefore, in the models used for this study I used three lines crossing the center of the phantom (Figure 2.1 and Figure 2.2). The lines along x axis were constrained to have no displacement in y direction and the lines along y axis were constrained to have no displacement in x direction. The vertical lines were confined along z axis.

To extract the 3D ideal displacement fields simulated by the FEM software, I created a MATLAB routine. The FEM software generated MATLAB code for mechanical simulation, including all the mechanical parameters of the model. Then the code was run by the MATLAB interface provided by the FEM software and the displacement solution vectors of the model would be available in the workspace of MATLAB. The ideal displacement fields were reorganized into 3D volumes and used as the input of the RF simulation. Because the simulated motion is three-dimensional, the simulation result consisted of three volumes: an axial displacement volume, a lateral displacement volume and an elevational displacement volume. The ideal axial and axial-shear strain distributions were also extracted from the FEM results as a reference to later compare the simulated elastograms.

For the purpose of illustration, Figure 2.3 shows the cross sections of displacement field and strain field in a uniform simulated medium under 1% strain. These frames represent the ideal displacement distribution of the 3rd off-set frames (0.9375mm) form the center in elevational direction. Figure 2.4 shows the ideal displacement and strain distribution in the simulated medium containing a spherical inclusion subjected to1% strain.

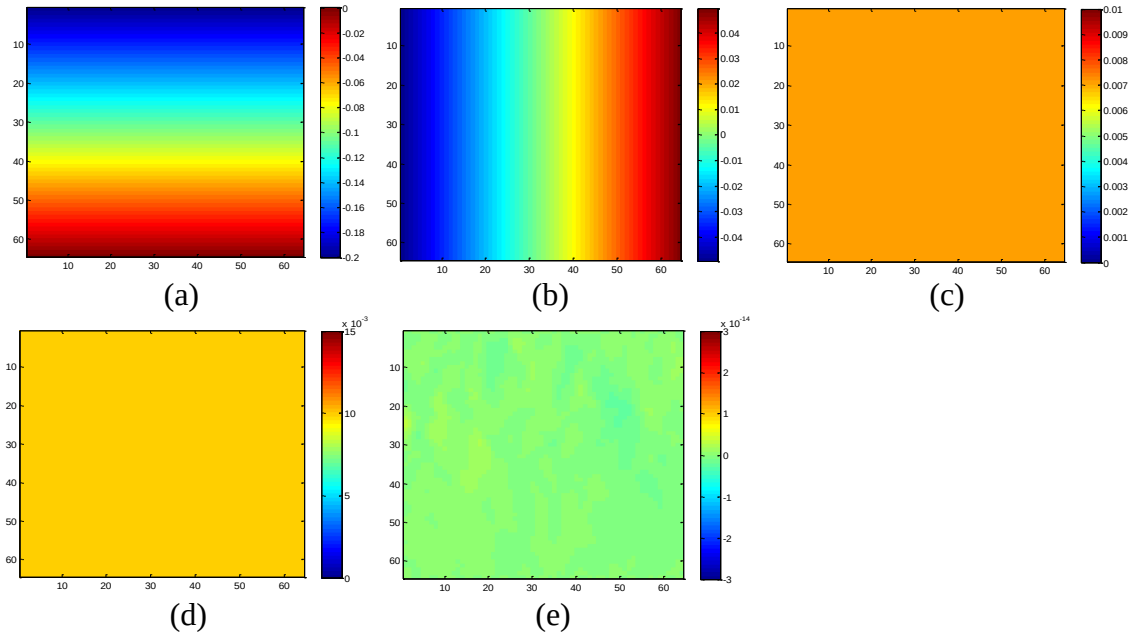

Figure 2.3 Ideal displacement and strain distributions in a simulated uniform medium subjected to 1% applied strain: (a) axial displacement (b) lateral displacement (c) elevational displacement (d) axial strain (e) axial-shear strain
The images refer to a cross-section spaced 0.9375mm from the geometric center of the phantom

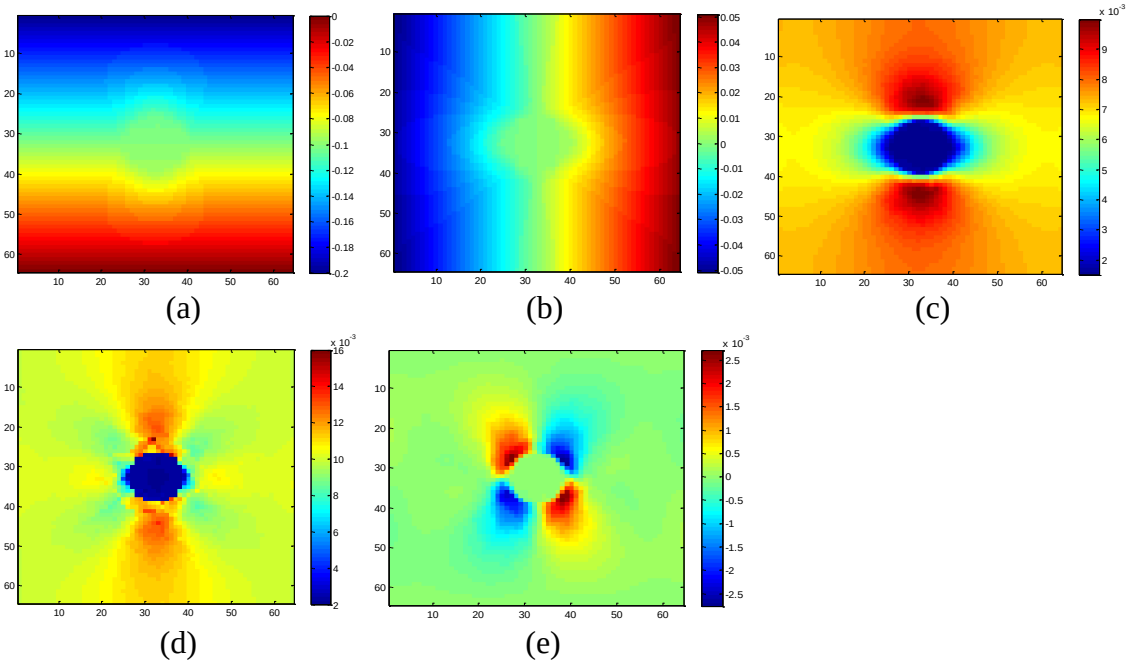

Figure 2.4 Ideal displacement and strain distributions in a simulated medium containing spherical inclusion subjected to 1% applied strain: (a) axial displacement (b) lateral displacement (c) elevational displacement (d) axial strain (e) axial-shear strain
The images refer to a cross-section spaced 0.9375mm from the geometric center of the phantom

2.2 RF Simulation

2D RF simulation software is widely used in the US elastography research (Righetti and Ophir 2002, Righetti et al. 2003, Srinivasan et al. 2003). These algorithms assume all displacements generated by the compression are constrained within a single plane. Because the out-of-plane motion could be source of significant decorrelation between the pre- and post- compression RF frames, the RF data generated using 2D simulations may result in an overoptimistic estimation of elastographic image quality. To perform more realistic image quality analysis of elastography performance, a 3D RF simulation software is created and used in this work.

The RF simulation software generated and used in this thesis is based on the convolution theory and it is an extension of the 2D RF simulation software previously developed in our laboratory (Chaudhry 2010). This software makes several simplifying assumptions. First, it assumes that the point spread function (PSF) of the system is linear and the whole region of interest (ROI) is at the focus of the US beam, where the PSF can be regarded as shift-invariant. In this condition, the echo signal can be represented as the convolution between the system PSF and the tissue scattering function (Konofagou and Ophir 2000). Second, the PSF is assumed separable, which is also valid only at the focus (Konofagou and Ophir 2000). Third, the scattering amplitudes inside the material are modeled as independent and identically distributed Gaussian random variables in a 3D space. Therefore, the inclusion and background have similar acoustic properties. Under the external compression, the scattering distribution changes depending on the

mechanical properties of the material. This can be obtained by redistributing the tissue scatterers based on the displacement field provided by the mechanical simulation model. At last, multiple scattering and ultrasound attenuation are both neglected in this RF simulation software. Although simplistic, similar models have been widely used in the elastography literature (Konofagou and Ophir 2000, Patil et al. 2008).

Analytically, the 3D PSF can be written as:

$$p(x, y, z) = p_a(y)p_l(x)p_e(z) \tag{3.1}$$

where x, y and z are lateral, axial and elevational coordinates, respectively. The PSF can be decomposed into three parts: $p_a(y)$, $p_l(x)$ and $p_e(z)$, which are the axial, lateral and elevational PSF components, respectively.

The axial PSF component can be modeled as a Gaussian modulated cosine pulse:

$$p_a(y) = A\exp(-\frac{y^2}{2\sigma_y^2})\cos(\frac{2\pi y}{\lambda}) \tag{3.2}$$

where A is a constant, λ is the central wavelength of the US system and σ_y is the pulse length. The lateral and elevational PSF components can also be modeled as Gaussian functions:

$$p_l(x) = \frac{1}{\sqrt{2\pi\sigma_x}}\exp(-\frac{x^2}{4\sigma_x^2}) \tag{3.3}$$

$$p_e(z) = \frac{1}{\sqrt{2\pi\sigma_z}}\exp(-\frac{z^2}{4\sigma_z^2}) \tag{3.4}$$

where σ_x and σ_z are the lateral and elevational correlational lengths, respectively. The pre- and post-compression 3D RF echo signals at each point in the simulated media can then be obtained using a convolution model:

$$r_1(x,y,z) = p(x,y,z) * t_1(x,y,z) + n_1(x,y,z) \tag{3.5}$$

$$r_2(x,y,z) = p(x,y,z) * t_2(x,y,z) + n_2(x,y,z) \tag{3.6}$$

where $n_1(x,y,z)$ and $n_2(x,y,z)$ are independent zero-mean white noise sources, $t_1(x,y,z)$ is the pre-compression tissue scattering function and $t_2(x,y,z)$ is the post-compression scattering function, which is given by:

$$t_2(x,y,z) = t_1(x-u(x), y-v(y), z-w(z)) \tag{3.7}$$

where $u(x)$, $v(y)$ and $w(z)$ are the lateral, axial and elevational displacement distributions provided by the mechanical simulation tool.

In this thesis, I simulated a 2D transducer array, which had a size of 64×64 pixels. The central frequency of the simulated ultrasound system was 6.5MHz and the bandwidth was 50%. The beamwidth of the transducer was assumed dependent on the wavelength and to be approximately 1 mm at 6.5MHz. The sampling frequency was 40MHz. The speed of sound was set as a constant of 1540 m/s in all cases. To meet the requirement of the Rayleigh scattering, a scatterer density of at least 40 scatterers per pulse-width was used. The sonographic signal-to-noise ratio (SNR_s) of the fundamental signals was set as 40dB.

A bilinear interpolation technique was used to compute the exact location of the scatterers after compression. A diagram summarizing the various steps of the RF simulation software is provided in Figure 2.5.

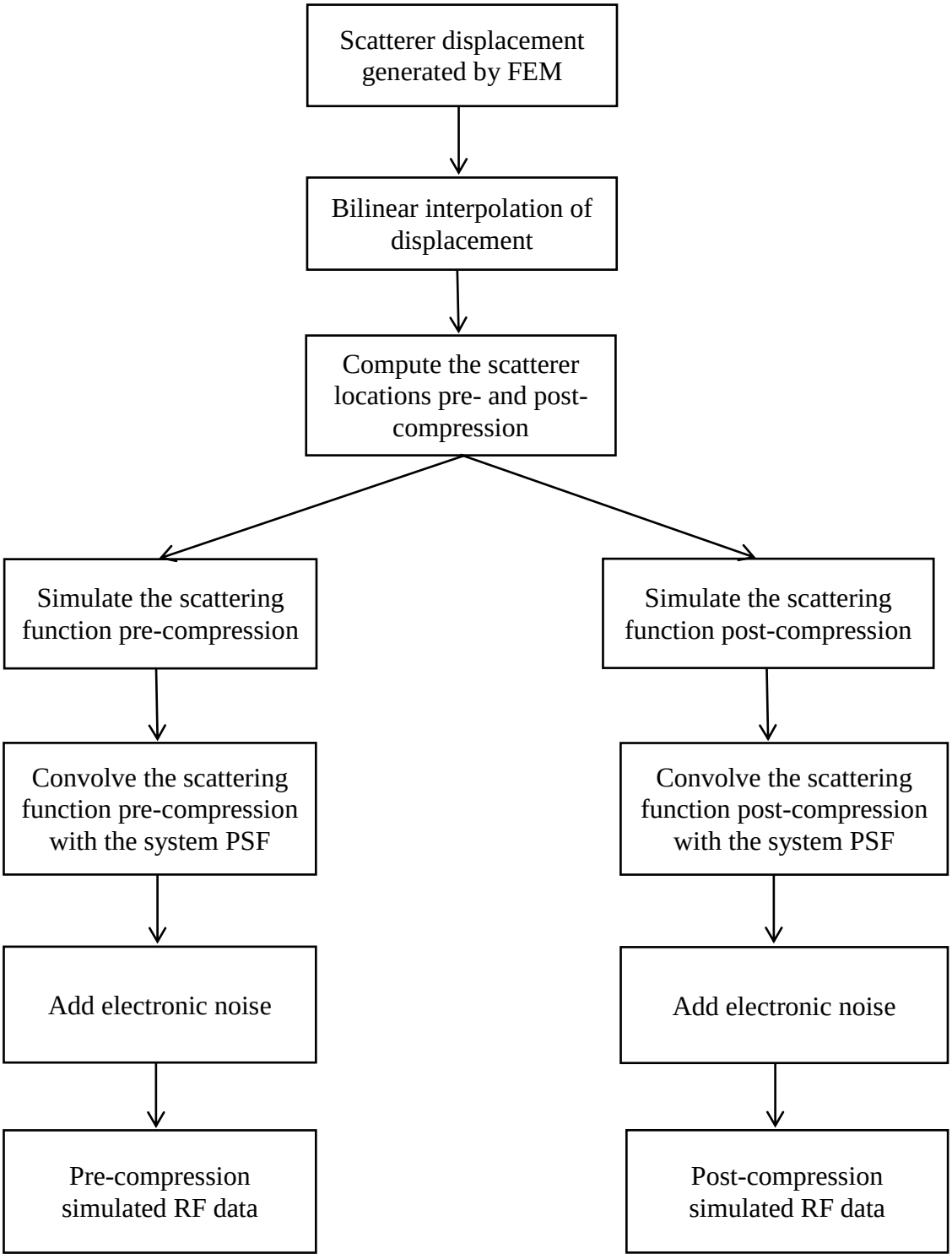

Figure 2.5 Diagram of the RF simulation software implemented in this study

CHAPTER III

THREE-DIMENSIONAL ELASTOGRAPHY ALGORITHM

The tissue motion estimator developed in this work is an extension of 2D block-matching methods (Yeung et al. 1998). This 3D volume-matching technique selects a small volume from the pre-compression RF data and a larger volume from the post-compression RF data. Both volumes have their centers at the same location in the RF data sets. The 3D elastography algorithm then computes the normalized cross-correlation function between the two volumes and finds out its maximum value, whose position is an estimate of the displacement between the two volumes. Nevertheless, under external compression, the tissue scattering function will not only be shifted, but also be temporally downscaled. So a global stretching is applied prior to the volume-matching to increase the correlation between pre- and post- compression data (Alam and Ophir 1997). After the displacement volumes are obtained, staggered strain estimator is used to compute the strain tensors (Srinivasan et al. 2002b). The various steps of the 3D volume-matching elastography algorithm are shown below:

- Globally stretch the post-compression RF data
- Select a 3D window V_1 and a larger 3D searching area V_2 from the pre- and post-compression data, respectively
- Compute the normalized cross-correlation function between V_1 and V_2
- Find out the location of the peak of the normalized cross-correlation function

- Apply spline interpolation to obtain sub-sample estimation
- Apply medium filtering on the displacement volumes
- Apply the staggered strain estimator to obtain axial strain and axial-shear strain estimates

3.1 Temporal Stretching

There are two main sources of time delay estimation error in elasticity imaging. The first one is the electronic random noise and the second source is the decorrelation of the RF signal due to tissue compression (Céspedes I et al. 1997). The effect of decorrelation is that the expected cross-correlation function between the pre- and post- compression signals is a filtered version of the autocorrelation function of the pre-compression signal.

The pre- compression RF signal can be modeled as (Konofagou and Ophir 2000):

$$\mathrm{r_1(x,y,z) = s(x,y,z) * p(x,y,z) + n_1(x,y,z)} \tag{4.1}$$

where $s(x,y,z)$ is the scattering function of the tissue, $p(x,y,z)$ is the PSF of the US system and $n_1(x,y,z)$ is independent zero-mean white noise source. The scatterers are redistributed due to the applied external compression. The post- compression RF signal can be modeled as (Alam and Ophir 1997):

$$\mathrm{r_2(x,y,z) = s\left(\frac{x}{a} - x_0, y - y_0, z - z_0\right) * p(x,y,z) + n_2(x,y,z)} \tag{4.2}$$

where $n_2(x, y, z)$ is noise source uncorrelated with $n_1(x, y, z)$ and the scaling factor a has a relationship with the applied strain ε (Alam and Ophir 1997):

$$a = 1 - \varepsilon \tag{4.3}$$

The external compression yields three-dimensional deformation of the tissue. However, because for an US imaging device, the lateral and elevational resolutions are much lower than the axial resolution, the scaling effects in the lateral and elevational directions can be neglected, and only the translational shifts are taken into consideration (Deprez et al. 2009). If the post- compression RF data is temporally stretched in the axial direction by a factor of a, then we obtain:

$$r_3(x, y, z) = r_2(ax, y, z) = s(x - x_0, y - y_0, z - z_0) * p(ax, y, z) + n_3(x, y, z) \tag{4.4}$$

where $n_3(x, y, z)$ is a scaled version of $n_2(x, y, z)$. The temporal stretching can largely increase the correlation between pre- and post- compression RF data, thus decrease the noise in elastograms (Alam and Ophir 1997, Varghese et al. 1996). For small compression, temporal stretching almost completely offsets the decorrelation caused by tissue compression. For the purpose of illustration, Figure 3.1 shows the effect of temporal stretching on a simulated RF signal.

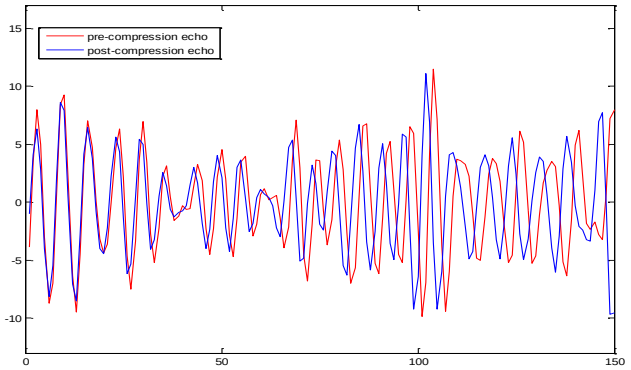

(a)

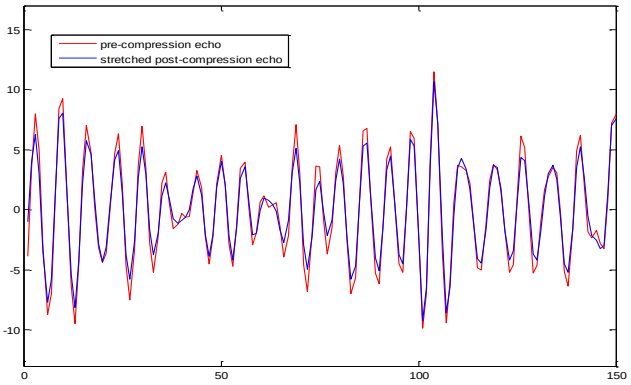

(b)

Figure 3.1 Example showing the effect of temporal stretching in elastography (a) pre- and post- compression RF signals before temporal stretching
(b) same signals after temporal stretching

Because the temporal stretching of the post-compression RF signal has an effect that decreases the displacement between the pre- and post- compression RF signals, the time delay estimation based on the stretched post-compression RF signal results in an underestimation of scatterer motion. Therefore, after the time delay estimation is completed, the effect of temporal stretching should offset. This is implemented by adding a compensational displacement field to the estimated displacement field. The compensational displacement field does not change in either the lateral or the elevational

direction, but linearly increases in the axial direction with a factor ε, which means a larger axial displacement is compensated in the deeper area inside the mechanical model.

3.2 Time Delay Estimation (TDE)

Once the temporal stretching is applied to the post-compression RF data, the two sets of echo signals are divided into many overlapping volumes and time delay estimation (TDE) methods are applied to estimate the local displacements. A 3D window $V_1(x, y, z)$ centered at (x_i, y_i, z_i) is picked out from the pre-compression data and a larger 3D searching area $V_2(x, y, z)$ also centered at (x_i, y_i, z_i) is picked out from the stretched post-compression data. The sizes of these two 3D windows are determined as a compromise between two factors: resolution and signal-to-noise ratio of the resulting elastogram (Srinivasan et al. 2003). To achieve a higher resolution, smaller windows are preferable, while larger windows will in general provide higher signal-to-noise ratios. In this thesis, I did not analyze the effect of window length on the resulting elastograms. However, based on prior work carried out in our laboratory, a 3D window of 1.25 mm (axial) × 1.25 mm (lateral) × 1.25 mm (elevational) was found to provide a good compromise between resolution and signal-to-noise ratio (1.25 mm in axial direction means a window contains about five wavelengths). The size of the searching area was set to 1.64 mm (axial) × 1.875 mm (lateral) × 1.875 mm (elevational).

The time delay between the window and the searching area is then estimated, and the result is the displacement vector at the location of (x_i, y_i, z_i). The window and the searching area are then moved to the next location $(x_i + \Delta x_i, y_i + \Delta y_i, z_i + \Delta z_i)$, and the TDE is performed again. The overlap between two successive windows is typically 80% (axial) and 75% (lateral and elevational). This procedure is repeated until the whole ROI has been covered.

The TDE method used in this study is the well-known correlation method, which is based on finding out the maximum value of the normalized cross-correlation (NCC) function. Although many similarity criterion functions can be used, such as the sum of squared difference (SSD) and the sum of absolute difference (SAD), the NCC is most widely used in elastography (Ophir et al. 1991, Varghese and Ophir 1996, Alam et al. 1998, Konofagou and Ophir 2000, Srinivasan et al. 2002b, Deprez et al. 2008, Deprez et al. 2009). A recent study performed in our laboratory has demonstrated that the NCC is the most accurate and stable TDE technique when compared to a number of other similarity criterion functions in elastography applications. The NCC can be computed using the fast Fourier transform (FFT), which reduces the computational burden. The NCC between $V_1(x, y, z)$ and $V_2(x, y, z)$ is given by:

$$C_{12}(x', y', z') = \frac{\sum_{x,y,z} \widetilde{V_1}(x,y,z) \cdot \widetilde{V_2}(x+x', y+y', z+z')}{\sqrt{\sum_{x,y,z} (\widetilde{V_1}(x,y,z))^2 \cdot \sum_{x,y,z} (\widetilde{V_2}(x+x', y+y', z+z'))^2}} \tag{4.5}$$

where $\widetilde{V_i}(x, y, z) = V_i(x, y, z) - \bar{V}_i(x, y, z)$, and $\bar{V}_1(x, y, z)$, $\bar{V}_2(x, y, z)$ are the mean values of the window and the searching area, respectively. The maximum value of the

NCC is found using exhaustive searching and its relative location to the NCC volume center, denoted as (x_M, y_M, z_M), is regarded as the estimate of displacement (axial, lateral, and elevational). However, to achieve sub-sample resolutions, the $3 \times 3 \times 3$ neighboring volume of the NCC peak is interpolated using a 3D spline interpolation (Yeung et al. 1998). In this study, the interpolation factors in the three directions are: 100:1 for axial direction, 10:1 for both lateral and elevational directions. Because the axial displacement is used for both the axial strain and axial-shear strain estimations, the interpolation factor in this direction is set high enough to obtain fine resolution in the resulting image. Since the lateral and elevational displacements are not the objective of this thesis, the interpolation factors in the lateral and elevational directions are set relatively low to reduce the computational time. The maximum value of the interpolated neighboring volume is found by exhaustive searching and its relative location to the center of neighboring volume (x'_M, y'_M, z'_M) is obtained. Therefore, the displacement estimate with sub-sample resolution $(x_{SSM}, y_{SSM}, z_{SSM})$ can be given by:

$$(x_{SSM}, y_{SSM}, z_{SSM}) = (x_M, y_M, z_M) + (x'_M, y'_M, z'_M) \tag{4.6}$$

3.3 Staggered Strain Estimation

Conventional strain estimation techniques (CSE) compute the strain as the gradient of the displacement field obtained through the NCC between pre- and post- compression RF signals (the relationship between the strain tensor and the displacement is listed in

the appendix). However, simple gradient methods are too noisy for elastography applications. To overcome some of the limitations of simple gradient techniques, a staggered strain estimation technique (SSE) has been proposed in the past (Srinivasan et al. 2002b). A similar SSE technique has been implemented and used in this thesis.

The SSE implemented in this thesis is a multistep algorithm. First, an elastogram is computed using non-overlapped windows. Then the windows are shifted by a distance that is a small fraction of the window size, and a new elastogram is computed. This process is repeated for all windows in the ROI. At last, the strain estimates of all the steps are staggered based on the location of each window to produce the final elastogram. The SSE results in a significant improvement in the SNR_e and CNR_e at high window overlap over CSE.

CHAPTER IV

IMAGE QUALITY ANALYSIS AND THREE-DIMENSIONAL STRAIN FILTERS

4.1 Image Quality Analysis

The following parameters are computed to evaluate elastographic image quality.

4.1.1 Accuracy

Accuracy is defined as the absolute error between the estimated strain and the ideal strain. Only the error of axial strain and axial-shear strain estimates is evaluated in this thesis. For a computed 3D strain volume $\hat{s}(x,y,z)$, the absolute error between the estimated strain volume and the ideal strain volume $s(x,y,z)$ can be defined as:

$$e(x,y,z) = \left|\frac{\hat{s}(x,y,z)-s(x,y,z)}{s(x,y,z)}\right| \times 100\% \tag{5.1}$$

And the mean absolute error (MAE) of $\hat{s}(x,y,z)$ can be defined as:

$$e = \frac{1}{N}\sum_{x,y,z} e(x,y,z) = \frac{1}{N}\sum_{x,y,z}\left|\frac{\hat{s}(x,y,z)-s(x,y,z)}{s(x,y,z)}\right| \times 100\% \tag{5.2}$$

where N denotes the number of voxels in the volume $\hat{s}(x, y, z)$. Before computation of the absolute error, the strain estimate needs to be interpolated into the same size as the ideal strain.

4.1.2 Elastographic Signal-to-Noise Ratio (SNR_e)

The SNR_e is defined for uniform materials as the ratio of the mean value of the estimated strain (μ_s) to the standard deviation of the estimated strain (σ_s) (Céspedes and Ophir 1993):

$$SNR_e = \frac{\mu_s}{\sigma_s} \tag{5.3}$$

The SNR_e is a measure of relative noise level in the image.

4.1.3 Elastographic Contrast-to-Noise Ratio (CNR_e)

The CNR_e is a measure of the detectability of a target. In elastography, CNR_e has been defined as (Bilgen and Insana 1997):

$$CNR_e = \frac{2(\mu_t - \mu_b)^2}{\sigma_t^2 + \sigma_b^2} \tag{5.4}$$

where μ_t and μ_b are the mean values of the estimated strain in the target and the background respectively, and σ_t and σ_b are the standard deviations of the estimated

strain in the target and the background respectively. In this thesis, the CNR_e is computed in the simulated media with spherical inclusion.

4.1.4 Axial-shear Strain Contrast-to-Noise Ratio ($\mathrm{CNR_{asse}}$)

The axial-shear strain contrast-to-noise ratio has been defined as (Konofagou and Ophir 2000):

$$CNR_{asse} = \frac{2(\widehat{\mu_t} - \widehat{\mu_b})^2}{\widehat{\sigma_t^2} + \widehat{\sigma_b^2}} \tag{5.5}$$

where $\hat{\mu}$ denotes the average and $\hat{\sigma}$ denotes the standard deviation. The subscripts 't' and 'b' stand for the target and the background, respectively. Although this definition appears similar to the CNR_e, there are some significant differences. In the case of a single spherical inclusion, the target in the axial-shear strain image is defined as the peak of the profile taken along the 45° orientation with respect to the axis of compression (Konofagou and Ophir 2000). The background can be a region far from the interface. For the model with a single spherical inclusion, the background is chosen as the center of the image because it is expected to have zero value (see also Figure 4.1). The mean and the standard deviation of the strain estimates are computed at the same location but over a number of independent realizations (Konofagou and Ophir 2000).

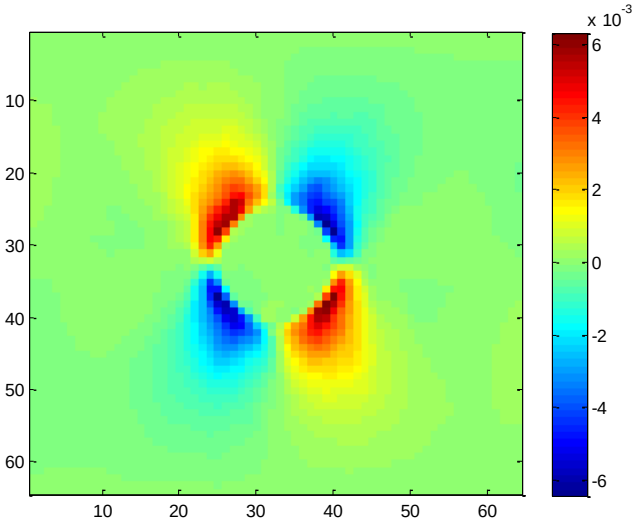

Figure 4.1 The ideal axial-shear strain of a model containing a single spherical inclusion The inclusion is three times stiffer than the background and the compression is 1% applied axial strain

Although the definition of axial-shear strain signal-to-noise ratio (SNR_{asse}) has also been established in the literature (Konofagou and Ophir 2000), the evaluation of the SNR_{asse} is not included in this thesis for the following reason. The formula of the SNR_{asse} is given by (Konofagou and Ophir 2000):

$$SNR_{asse} = \frac{\hat{s}_{asse}}{\hat{\sigma}_{asse}} \tag{5.6}$$

where $\hat{s}_{asse}$ is the estimated mean of the axial-shear strain estimates and $\hat{\sigma}_{asse}$ is the standard deviation of the axial-shear strain estimates. In general, a measurement of the signal-to-noise ratio should be performed on a uniform strain image with non-zero mean value. A uniform simulated medium under axial compression yields a constant axial-shear strain equal to zero.

4.2 Three-dimensional Elastographic Strain Filter

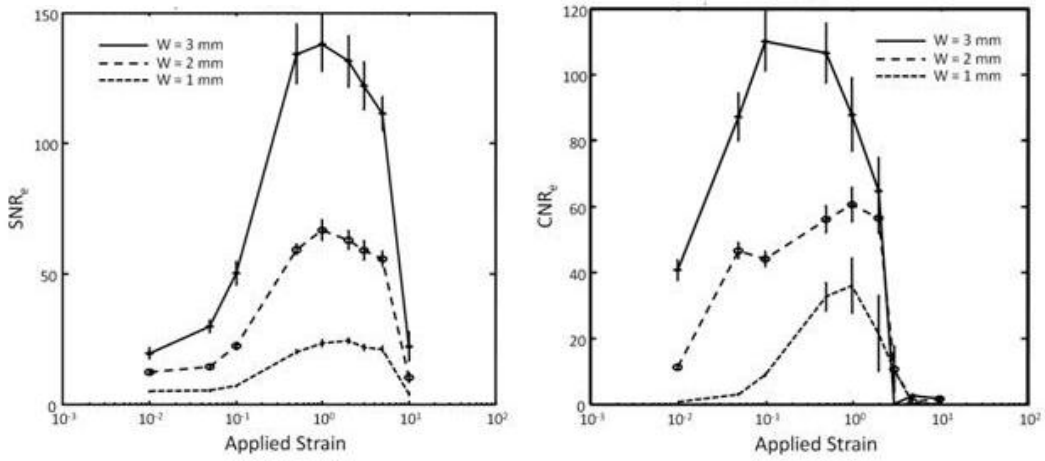

(a) (b)

Figure 4.2 (a) SNR_e strain filter with different window length (b) CNR_e strain filter with different window length (with the courtesy of Yang, Xu)

The strain filter is a term used to describe the nonlinear filtering process in the strain domain that allows the elastographic depiction of a limited range of strain from the compressed tissue (Varghese and Ophir 1997). It shows the behavior of the SNR_e or CNR_e as a function of axial tissue strain in the strain domain. Ideally, the strain filter has an infinitely high, flat all-pass characteristic in the strain domain. However, in real conditions, the strain filter has a band-pass shape (Varghese and Ophir 1997, Srinivasan et al. 2003, Thitaikumar et al. 2007, Patil elt al. 2008). The low values of the strain filter in low strain conditions are primarily due to weak signal and relatively high electronic noise (i.e. the low SNR_s). At high strain values, the drop in the performance of elastography algorithm is caused by strong decorrelation of RF signals. For the purpose of illustration, Figure 4.2 shows examples of SNR_e and CNR_e strain filter.

The strain filter predicts the elastographic image quality under certain tissue condition and parameters of signal processing and ultrasound system used to generate the elastogram (Varghese and Ophir 1997). Signal decorrelation determines the largest value of strain that can be accurately estimated, while the SNR_s determines the smallest measurable strain value. Inversely, the strain filter helps to select appropriate signal processing and ultrasound system parameters to obtain the best possible elastogram under given tissue conditions.

Conventionally, strain filters are used to analyze only 1D or 2D elastography techniques. In this work, a 3D simulation method is used to generate the RF signals with elevational displacement, in order to have a more realistic estimation of the performance of elastography algorithm.

In this work, the strain filters are not only investigated under different strain values but also at different frame locations in the simulation media. This allows generation of '3D strain filters', which can be used to evaluate image quality of 3D algorithms with respect to strain and frame location. For comparison, the SNR_e, CNR_e and CNR_{asse} of the central frame and three off-set frames are evaluated and statistically compared. It can be expected that image quality will decrease as the off-set number becomes larger, because more transverse displacements exist as we move away from the center of the phantom. Furthermore, a comparison between a 2D elastography technique (block matching) and the 3D elastography technique is provided. Since the 3D technique estimates the elevational motion of scatterers, we can expect the 3D technique to be more accurate.

In this thesis, each strain filter (for SNR_e, CNR_e and CNR_{asse}) includes nine different strain values. Under each strain value, ten sets of independent RF data consisting both the pre- and post- compression RF signals, are computed using a single mechanical model. 2D and 3D elastography techniques are applied to estimate the strain distributions. The SNR_e and CNR_e in different frame positions are computed and then the average of ten realizations and then used to compute the 3D strain filters. For the CNR_{asse}, because the definition of this parameter is distinct from the definitions of SNR_e and CNR_e, the computation of the strain filter requires some modifications (Thitaikumar et al. 2007). A pixel for the target and a pixel for the background are picked out from each of the ten realizations, then the mean and the standard deviation of the target and background are calculated to obtain the CNR_{asse}. That is to say, the ten realizations yield a single value of CNR_{asse}, rather than the average of CNR_{asse}, which is the case for SNR_e and CNR_e.

4.3 Statistical Analysis of 3D Elastography Algorithm

To evaluate the effectiveness of the 3D elastography algorithm, a statistical comparison between performance of 3D and performance of 2D techniques is carried out in this thesis. The student's t-tests is performed to discern the significant difference between the strain filters of 3D and 2D elastography techniques.

CHAPTER V

RESULTS AND DISCUSSION

In this chapter, I present the major results of my work. A demonstration of the simulated 3D elastograms is made at the beginning of the chapter followed by detailed analysis of the image quality of the 3D algorithm. A statistical comparison between the 3D elastography technique and the corresponding 2D elastography technique is also presented.

5.1 3D Elastograms

Figure 5.1 shows a 3D view of the estimated axial displacement, while Figures 5.2 and 5.3 show the corresponding 3D view of the estimated axial strain and axial-shear strain, respectively. A sphere inclusion model is used for this result. For these results, the Young's modulus of the inclusion was set at 3kPa and the applied strain was set at 1% (see Chapter II for details).

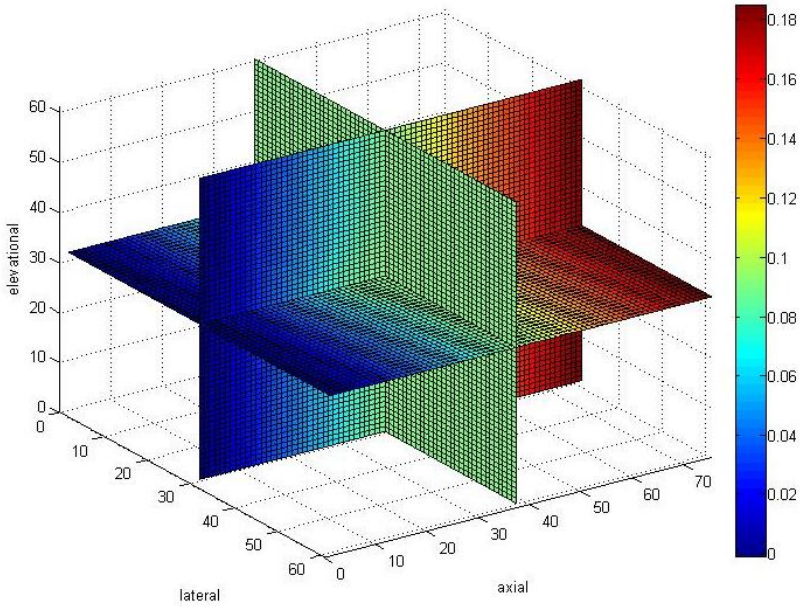

Figure 5.1 3D view of the axial displacement

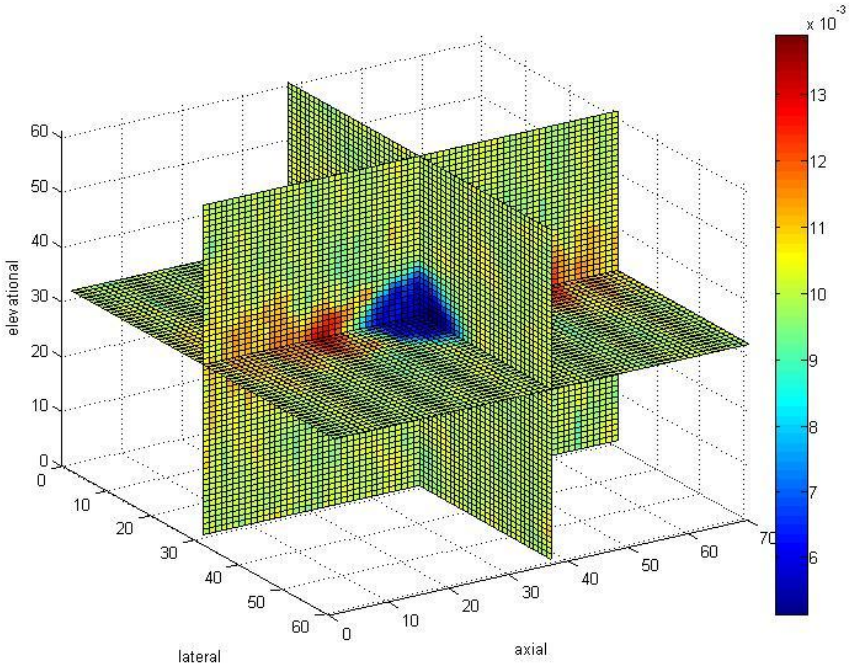

Figure 5.2 3D view of the axial strain

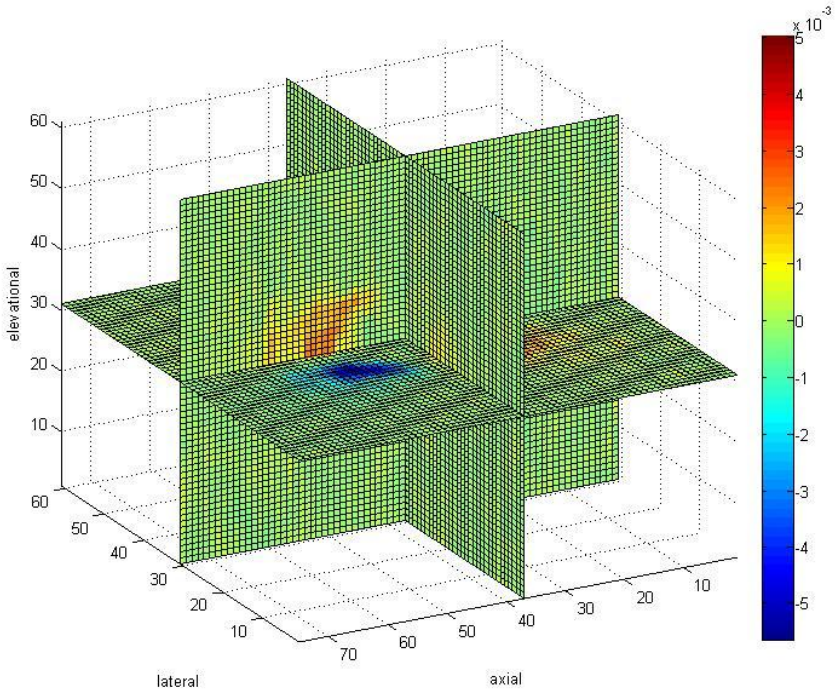

Figure 5.3 3D view of the axial-shear strain

In Figure 5.4, slices of the displacement fields of the 3D media are shown. The corresponding ideal displacement images computed by the FEM software are also shown for comparison.

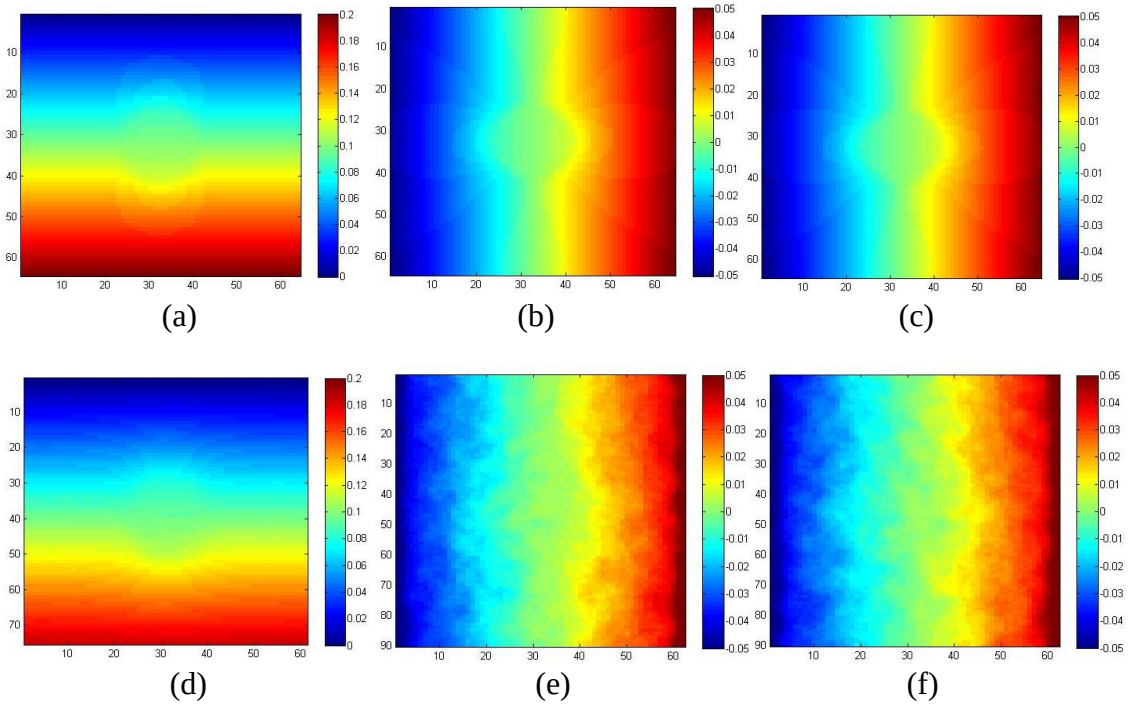

(a) (b) (c)

(d) (e) (f)

Figure 5.4 First row: ideal displacement (a) axial (b) lateral (c) elevational
Second row: estimated displacement (d) axial (e) lateral (f) elevational
Note: 1. (e) and (f) are results of averaging over ten realizations
2. the elevational displacements shown are in the central axial-elevational slice, while others are all in the central axial-lateral slice

From Figure 5.4, we can observe that the estimated axial displacement appears very similar to the ideal axial displacement, while the estimated lateral and elevational displacements are noisier than the axial displacement (Deprez et al. 2009). This is because in ultrasound, the axial estimation is much more accurate and precise than the lateral and elevational estimation. In addition, compared with the two transverse displacement components, the axial displacement image has more details in the inclusion area. The reason for this is that a much higher interpolation factor is applied in the axial direction than in the lateral and elevational directions in the TDE, leading to higher accuracy in the axial displacement image. Lateral and elevational estimation can be

improved by increasing the interpolation factors in the transverse directions. However, this would increase in the computational time significantly. Because the RF data has much lower resolution in the transverse directions, very high interpolation factors (larger than 100:1) should be used in the lateral and elevational cases. Since the 3D spline interpolation is the most time consuming step in the elastography algorithm, and the lateral and elevational displacement fields are used to improve correlation of the RF signals and make the axial displacement estimation more accurate and robust, in this thesis, relatively low interpolation factors are selected in the transverse directions. The average of the correlation coefficient in the entire 3D phantom is 0.9872, which is sufficiently large and the estimates of displacement are believable (Deprez et al. 2009).

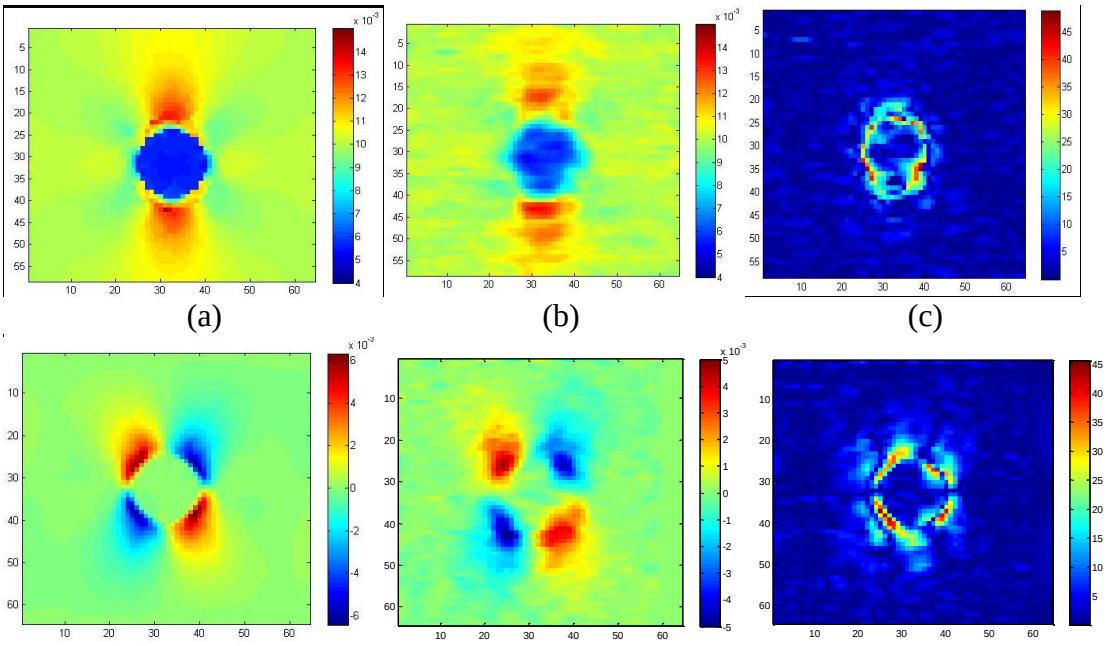

(a) (b) (c)

(d) (e) (f)

Figure 5.5 First row: axial strains (a) ideal (b) estimated (c) absolute error (%)
Second row: axial shear strain (d) ideal (e) estimated (f) absolute error (%)
Note: all the images are in the central axial-lateral slice

Figure 5.5 shows examples of simulated 3D elastograms. For comparison, the ideal strain images and corresponding absolute error maps are also shown. To obtain the absolute error map of axial strain, the difference between ideal and estimated axial strain images was computed by subtraction. Then the absolute value of the difference was divided by the ideal axial strain image. At last, the normalized difference was converted to percentage. The absolute error map of axial-shear strain estimate was computed in a similar method, but the normalization factor was not the ideal axial-shear strain image, because the background and inclusion have an expected value of zero. Instead, the difference was normalized by the applied strain. The absolute error map is essentially the relative difference between the ideal and the estimated image, and it is a measure of the accuracy of elastography algorithm. The average absolute error over the entire estimated axial strain volume and axial-shear strain volume were found to be 1.8581% and 1.4422%, respectively. It can be observed that although the 3D algorithm has relatively high accuracy in strain estimation in the background and inside the inclusion area, a relatively large error exits near the boundary. This is presumably an effect due to the window block used for the estimation. To increase the SNR of elastograms, the window should be several wavelengths (Srinivasan et al. 2003). However, when the window is located at the boundary between background and inclusion, the window contains both part of the background and part of the inclusion. This can lead to erroneous strain estimation at the boundary.

5.2 Errors under Different Strain Values and Frame Positions

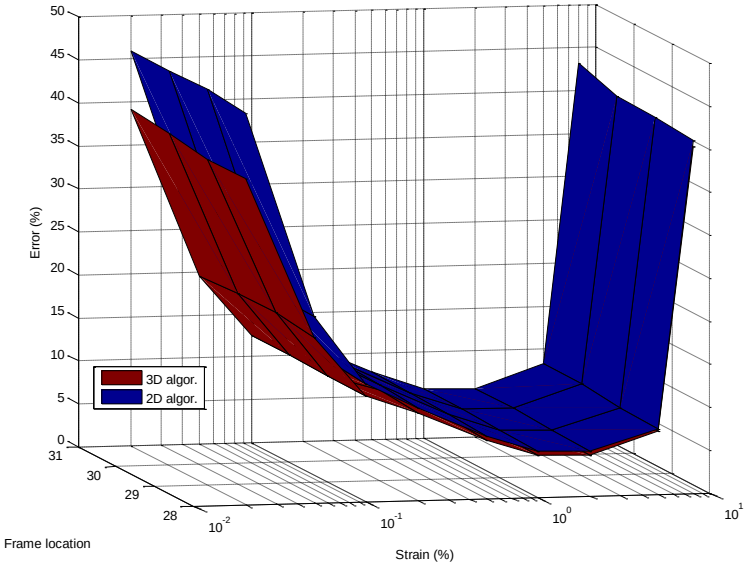

(a)

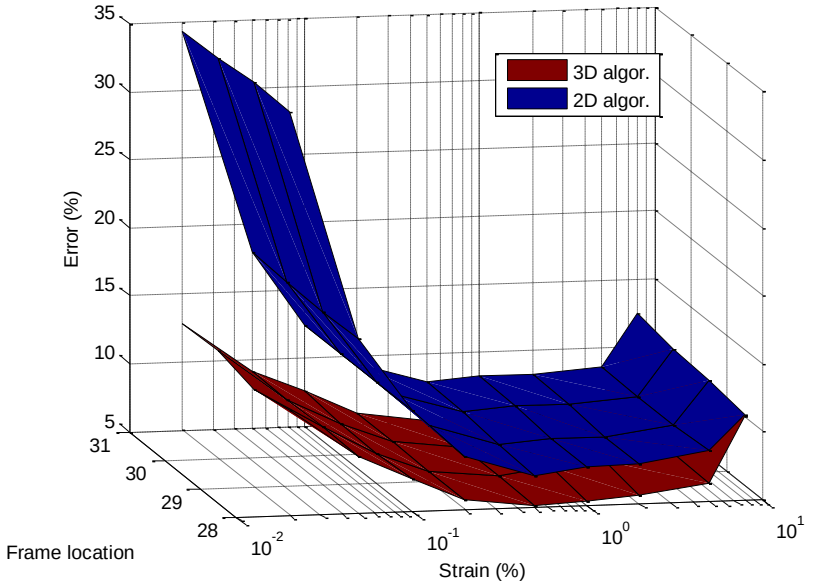

(b)

Figure 5.6 Errors under different strain values and frame positions
(a) axial strain error (%)
(b) axial-shear strain error (%)

Figure 5.6 shows the mean absolute errors of the axial strain estimates and the axial-shear strain estimates both for 3D technique and 2D technique as a function of the strain value and frame location. The mechanical model used for this analysis is the phantom with spherical inclusion. The Young's modulus of the inclusion was set to 10kPa. The same window size was used for the 3D and 2D estimations (1.25 mm for both the axial and lateral directions), while the window of 3D method was 1.25 mm in the elevational direction. Generally, the error associated with the 3D technique is lower than the error associated with the 2D technique both for the axial strain estimation and the axial-shear strain estimation. The error of 3D axial strain estimation becomes very high under small or large strain values, while is less than 10% if the strain is in the range of 0.2%~5%. The situation is similar for the axial-shear strain error. The difference in axial-shear strain error between the 3D estimation and 2D estimation is significant for low strain levels (<0.1%).

The behavior of the error can be explained using the strain filter theory (Varghese and Ophir 1997). When the phantom undergoes a large external compression, high decorrelation between the pre- and post- compression RF data occurs. For small strain values, the signal is weak compared to the electronic noise, which also deteriorates the accuracy of the strain estimation. The reason why 3D elastography might be more accurate than the 2D technique is that 3D elastography computes the deformation in the third dimension and is more robust in dealing with the noisy data than the 2D technique. I also computed error values of the central axial-lateral frame (31^{st} frame) and three parallel off-set frames (28^{th}, 29^{th}, 30^{th} frames). The distance between two successive

frames is 0.3335 mm. Under the same strain level, no notable difference in the error value between the central frame and the off-set frames is observed, both for 3D and 2D techniques.

5.3 3D SNR_e Strain Filter

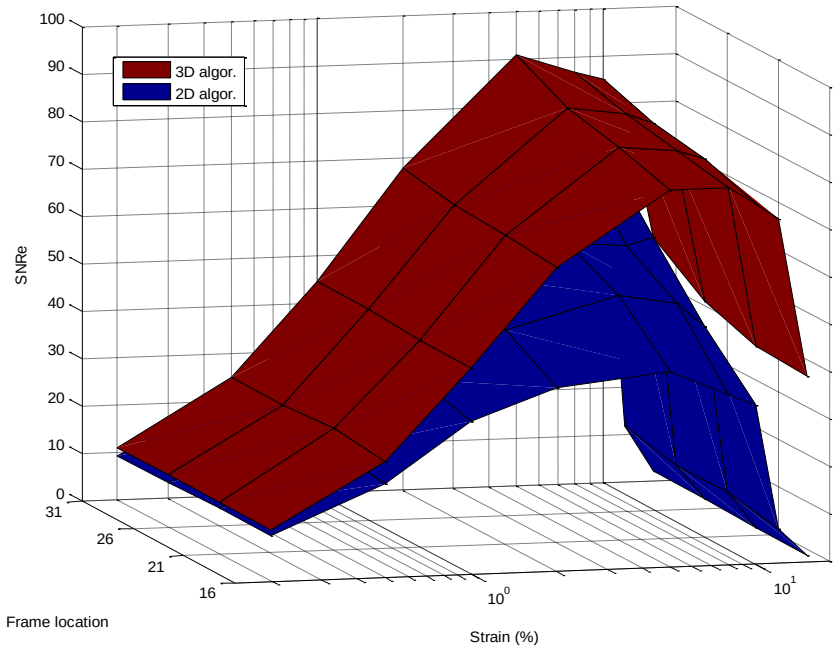

Figure 5.7 3D SNR_e strain filter

For the computation of SNR_e, uniform simulated media are used as specified in Chapter II. For each strain value, ten realizations are calculated. The SNR_e is computed as the average over these ten realizations. It can be observed that for both 2D and 3D elastography techniques, the SNR_e values form a band-pass shape in the entire strain domain. Both strain filters decrease gradually as the strain becomes smaller or larger

than 5%. Under the strain value of 15%, the two SNR_e strain filters have sudden drop, because the decorrelation entirely corrupts the elastogram. When the external strain is very small (~0.2%), the SNR_e values also become close to zero, because the SNR_s is small. In all conditions, the strain filter of the 3D technique has higher average value than the 2D technique does. The t-test shows, for all strain values and frame locations in Figure 5.7, the confidence levels or the p-values are less than 0.05, which means the strain filter of 3D technique is statistically significantly different from the strain filter of 2D technique. The difference in SNR_e is more significant in high strain levels. The reason is the elevational displacement could be a source of decorrelation between the pre- and post- compression RF signals. 2D elastography algorithm assumes no displacement exists in the elevational direction. Therefore, it suffers from the decorrelation caused by the elevational displacement and its image quality corrupts remarkably when the elevational displacement is large. The 3D elastography algorithm estimates all the three components of the motion inside the simulated medium, which reduces the decorrelation resulted from the elevational displacement. Therefore, the image quality of 3D elastography is better than that of 2D elastography, especially in large strain conditions.

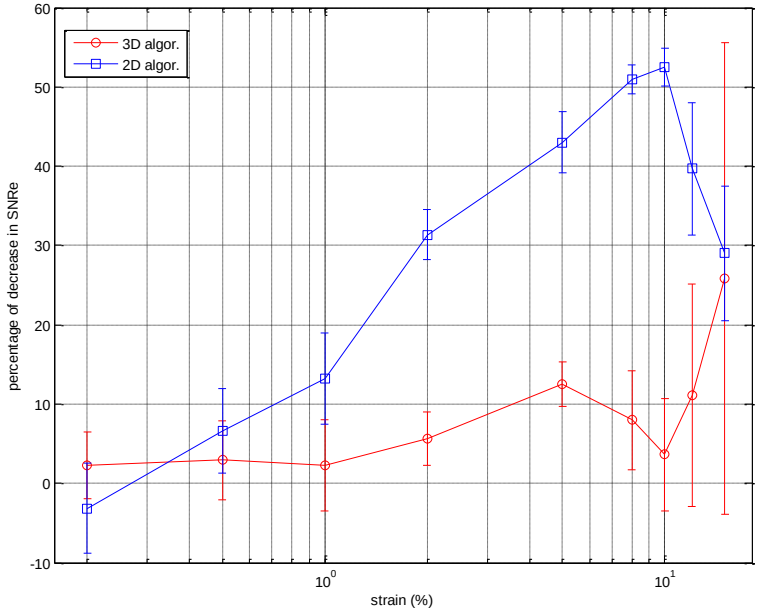

Figure 5.8 The decrease of SNR_e values between the central frame and the 3rd off-set frame (%)

From Figure 5.7 we can evaluate the SNR_e at different frame positions. The central axial-lateral frame (31st frame in Figure 5.7) and three parallel off-set frames (26th, 21st, 16th frames) are used. The distance between two successive frames is 1.667 mm. Figure 5.7 shows that the 3D technique has higher SNR_e in all frame locations than the 2D technique. For most of the cases, as the distance from the center of the simulated medium increases, the off-set frame has lower SNR_e value. This is due to larger transverse displacement, which exists as the phantom subjected to a uniform axial strain. Since the decorrelation of the RF data is a main source of noise in the strain estimate, axial-lateral slices far from the center have higher noise level compared to the central frame. The percentages of the decrease between the central frame and the 3rd off-set

frame in SNR_e both for 2D and 3D techniques are shown in Figure 5.8. In general, the 3rd off-set has lower SNR_e than the central frame (positive decrease values). When the strain becomes larger, the SNR_e decreases more significantly both for the 2D and 3D elastography techniques. Nevertheless, another advantage of the 3D algorithm, which estimates the elevational motion, is that it should be more robust in the strain estimation. This means when a large strain is applied, the image quality of 3D technique in a frame far from the center should be closer to the image quality of the central frame when compared with the 2D technique. This is verified by the result shown in Figure 5.8, which indicates that when the strain value is in the range of 0.5%~15%, the average decrease of ten realizations in the SNR_e between the central frame and the 3rd off-set is smaller when 3D elastography technique is used. The t-test shows that the two curves in the Figure 5.8 are statistically different in the range of 1%~12% strain, with the p-values less than 0.05.

5.4 3D CNR_e Strain Filter

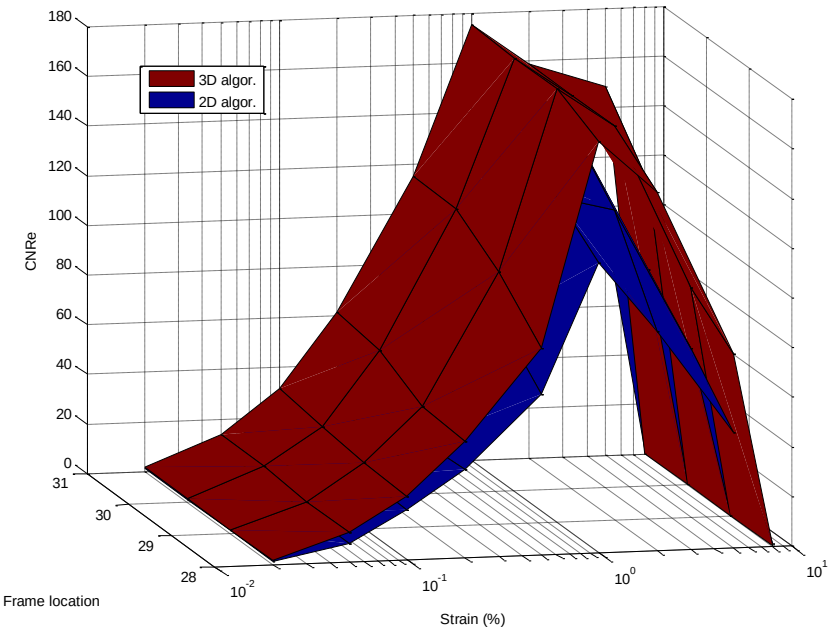

Figure 5.9 3D CNR_e strain filter

The 3D CNR_e strain filters of both the 2D and 3D elastography techniques are shown in Figure 5.9. The CNR_e values form a band-pass shape in the strain domain (Srinivasan et al. 2003, Patil et al. 2008). When the strain is small (0.02%~0.1%), the CNR_e values of both 2D and 3D techniques increase gradually as the strain becomes larger. On the other side of the strain filter, the CNR_e values drop quickly, because the decorrelation caused by the large strain corrupts the image quality of estimated strains. The 3D algorithm generally has higher average CNR_e values than the 2D algorithm. For large strain values (0.5%~5%), this difference becomes remarkable, because more decorrelation due to the external compression exits in these conditions. For very high strain values (larger than 8%), the elastograms corrupt and the CNR_e values drop to nearly zero both for 2D and

3D techniques. However, the t-test performed among the thirty-six points in Figure 5.9 (nine strain levels, four frames for each strain value) shows that only four points have a p-value less than 0.05. This means that no statistical difference exits between the CNR_e strain filters of 3D and 2D elastography techniques in general. This may be due to the fact that the CNR_e values of the ten realizations have fairly high standard deviations. Therefore, additional statistical tests may be required.

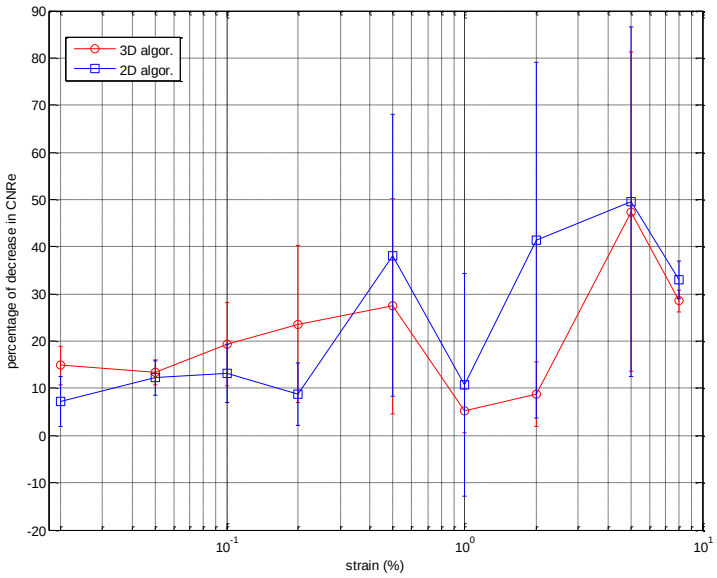

Figure 5.10 The decrease of CNR_e values between the central frame and the 3rd off-set frame (%)

The percentage of decrease in the CNR_e between the central frame (31st frame) and the 3rd off-set (28th frame) is displayed in Figure 5.10. In general, the 3rd off-set has smaller CNR_e than the central frame. Again, the reason for this is that the transverse displacements are greater in the off-set frame than in the central frame. In large strain conditions (larger than 0.5%), the effect of decrease is notable for both 2D and 3D

techniques, but the average percentage of decrease is slightly smaller for the 3D technique than for the 2D technique. The t-test indicates no statistical difference between the two curves shown in Figure 5.10.

5.5 3D $\mathrm{CNR}_{\mathrm{asse}}$ Strain Filter

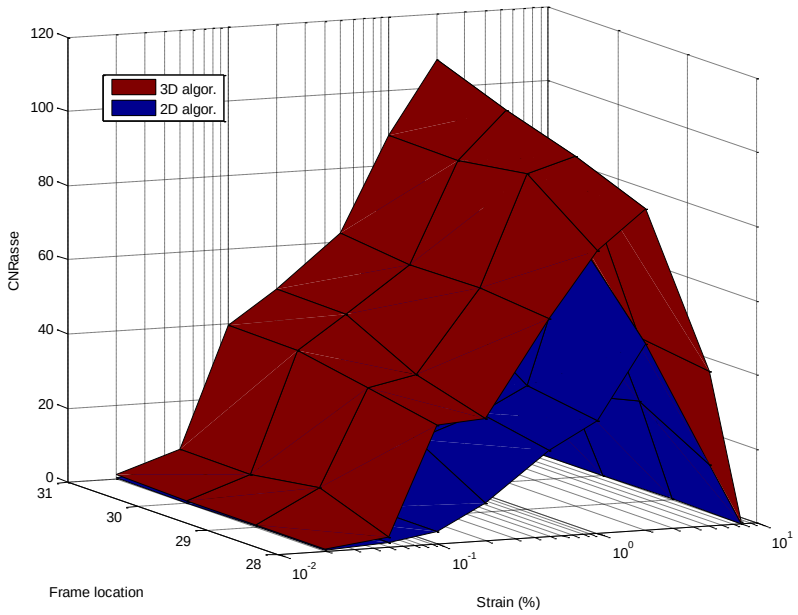

Figure 5.11 3D CNR_{asse} strain filter

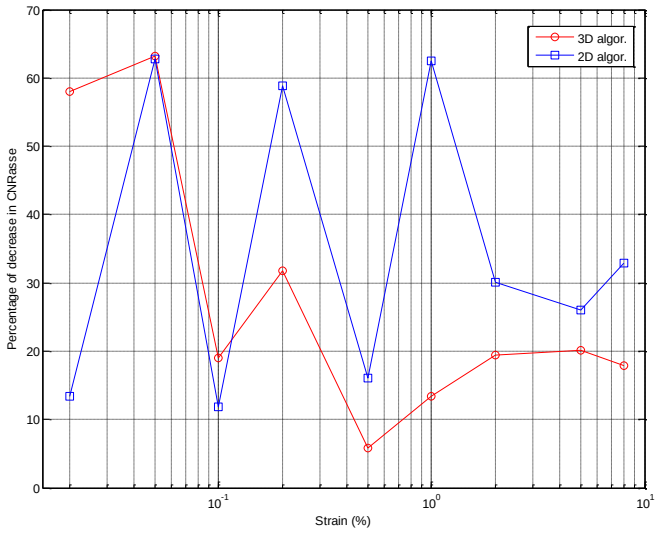

Figure 5.12 The decrease of CNR_{asse} values between the central frame and the 3rd off-set frame (%)

Figure 5.11 shows the 3D CNR_{asse} strain filters of both 2D and 3D elastography techniques. The strain filter of 2D technique has its peak at 1% strain, while the 3D technique has its peak at 2% strain. It should be noted that the average and standard deviation in the formula of CNR_e are computed on a single image, while their counterparts in the formula of CNR_{asse} are computed using ten individual realizations. Overall, the CNR_{asse} strain filter of the 3D algorithm has a larger value than the strain filter of the 2D algorithm. This seems to show that the 3D elastography technique is more effective in the axial shear strain estimation than the 2D technique, especially when the strain level is high.

Figure 5.12 provides the percentage of decrease in the CNR_{asse} values between the central slice (31st frame) and the 3rd off-set slice (28th frame). It can be observed that the decrease exits under all strain values, both for 2D and 3D techniques. However, the

decrease of the 3D algorithm is somewhat lower than the decrease of the 2D algorithm for most of the cases. This means, at locations that have larger elevational displacements and more decorrelation noise, the 3D elastography technique is more robust than the 2D technique.

Because for the CNR_{asse} strain filter, only one value is computed for a certain frame and strain value, the t-test is not applicable to discern the effectiveness of 3D and 2D techniques. And for the same reason, no error bars are displayed in Figure 5.12.

CHAPTER VI

CONCLUSIONS AND FUTURE WORK

6.1 Conclusions

The 3D elastography algorithm can effectively estimate the axial displacement in simulated media. The lateral and elevational displacement estimates are usually noisy, due to known ultrasound limitations (Deprez et al. 2009). The mean absolute error of the axial strain estimate computed using the 3D technique is smaller than 10% when the strain value is in the range of 0.2%~5%. When the strain is smaller than this range, the electronic noise becomes significant and the error becomes larger. On the other hand, high strain levels lead to large decorrelation in the RF data, hence increasing the error of the strain estimate. In the entire strain domain, the 3D algorithm has smaller mean absolute error than the 2D algorithm. No remarkable change in the mean absolute error is observed between different frame locations under the same strain value.

The computation of SNR_e, CNR_e and CNR_{asse} shows that these parameters have a band-pass behavior in the strain domain. The SNR_e strain filter reaches its maximum value at about 5% strain, the CNR_e reaches its maximum at about 1% strain and the CNR_{asse} strain filter reaches its maximum at about 2% strain. Because high strains lead to large decorrelation between the pre- and post- compression RF data, both CNR_e and CNR_{asse} drop quickly when the strain value becomes larger than 5%, and the SNR_e strain filter

has a steep slope under a strain of 12% or larger. The difference in these two threshold values is caused by the fact that the CNR_e and CNR_{asse} are computed using phantom with inclusion, while the SNR_e is computed using uniform phantom. For low strain conditions, because the SNR_s becomes small, the image quality of strain estimate deteriorates gradually. The comparison between the strain filters computed using the 3D elastography technique and the strain filters computed using the 2D elastography technique indicates that the former have higher average values in general. Especially, when the strain is large (0.1%~5% for CNR_e and CNR_{asse}, >1% for SNR_e), this difference becomes more remarkable. The t-test shows that the 3D algorithm is statistically superior to the 2D algorithm in term of the SNR_e in the entire strain domain. However, it also shows no statistical difference between the CNR_e strain filters computed using the 3D and the 2D techniques. This could be caused by the large standard deviation of the CNR_e results.

The SNR_e, CNR_e and CNR_{asse} are also computed at different elevational locations. It can be observed that as the distance of the frame from the center of the simulated medium increases, the values of SNR_e, CNR_e and CNR_{asse} reduces in general. This is due to the fact that higher transverse displacements exist in the area far from the geometric center of the phantom, which yields larger decorrelation in the RF signals in these areas. Results in the previous chapter demonstrate that both the 3D technique and the 2D technique show decreased SNR_e, CNR_e and CNR_{asse} in the off-set frames. For the average SNR_e decrease between the central frame and the 3rd off-set frame computed

from ten realizations, t-test indicates that if the strain is in the range of 2%~10%, the 3D algorithm is statistically more robust than the 2D algorithm.

In general, 3D elastography algorithm outperforms the 2D elastography algorithm. The 3D algorithm employs a 3D window and searching area for TDE, including the computation of elevational displacement, while the 2D technique only estimates the axial and lateral deformation. Since the elevational displacement could be an important source for the decorrelation in the RF data and noise in the strain estimate, the 3D technique is more effective and robust compared with the 2D technique, especially under high strain conditions.

6.2 Future Work

Several important work should be performed in the future. This work could improve the performance of the 3D elastography algorithm, in terms of both the time efficiency and resulting image quality and in general will provide better insight into the performance of 3D elastography algorithms.

6.2.1 Fast searching method or high dimensional surface parameter estimation

To obtain higher sensitivity in the displacement estimation, 3D spline interpolation is performed on a 3D neighboring area in the NCC function. The maximum values for both

the NCC function and the interpolated volume are found by exhaustive searching. These two steps are both highly time consuming. Because the elevational resolution of the RF signal is relatively low, intensive interpolation in this direction is applied and much more values of the NCC function have to be compared, which makes the 3D elastography algorithm remarkably slower than the 2D method. There are two measures to accelerate the 3D algorithm. Firstly, the exhaustive searching can be replaced by more efficient optimization method. Some other researchers have incorporated optimization algorithm in their elastography techniques (Po and Ma 1996, Basarab et al. 2008, Deprez et al. 2009). However, replacing the exhaustive search with a faster method cannot radically accelerate the 3D elastography algorithm, because the interpolation step is the bottleneck in the computational time of the 3D algorithm. Besides, the interpolation is a process with low efficiency, for only one value will be useful at the end of the computation. One alternative to get sub-sample resolution is the surface fitting technique. In this technique, the parameters of a three-dimensional surface that fits all the pixels in the 3D neighboring space are estimated and its maximum value is solved analytically. If polynomial surface is used, the parameters can be obtained by solving linear equations and the maximum value can be chosen among several local maximum or minimum values. The location of the maximum can also be calculated from the surface parameters. There are two advantages of this method. Firstly, it is not necessary to compute all the interpolated points in the neighboring space, which makes the algorithm more efficient. Secondly, the location of the maximum value can be computed directly from the surface parameters, so the sensitivity in the displacement will be higher than the interpolation

method, whose sensitivity is constrained by the interpolation factor. The surface fitting also has some drawbacks. The 3D neighboring space contains twenty-seven points, which means the order of the surface fitting all the points is high (if the order is 3, the linear equation will be under-constrained; if the order is 4, the linear equation will be over-constrained). The high order surface fitting may cause unstable results. Although some points in the neighboring space can be ignored to lower down the surface order, this may decrease the accuracy of the elastography algorithm.

6.2.2 Adaptive stretching of the RF data

Although the global stretching in the post-compression data can increase the correlation between the pre- and post- compression RF signals, the strain distribution is not uniform in most of the cases. In the areas that strain changes intensively, the global stretching may fail to correlate the pre- and post- compression data, and the resulting elastogram may suffer from high noise in these areas. A potential method to rectify this situation is to adopt the adaptive stretching (Alam et al. 1998, Srinivasan et al. 2002a), which stretches the post-compression data individually in each window rather than using a constant stretching factor for the entire ROI. This method may be very helpful in dealing with the problems of estimating the displacements near the boundary between two types of materials with large difference in stiffness.

6.2.3 Revise the definition of $\mathrm{SNR}_{\mathrm{asse}}$

As mentioned in Chapter V, the definition of the SNR_{asse} is problematic and its computation is not included in this thesis. However, since the SNR is an important measure of image quality and axial-shear strain provides clinically useful information, the application of SNR_{asse} would be inevitable in the research of elastography. The dilemma of the SNR_{asse} could be overcome by revising its definition. One possible method is that the SNR_{asse} be computed in a similar way with the CNR_{asse}. A number of realizations with non-zero area in the axial-shear strain image are computed and a pixel from the profile is picked out from each realization. The SNR_{asse} could be defined as the ratio of the average of these pixels to the standard deviation of them.

6.2.4 Experimental validation

No experimental elastogram has been provided in this thesis due to time constraints. However, experiments should be performed in the future to corroborate the simulation results.

As mentioned in Chapter I, the application of 2D array transducer facilitates the 3D elastography algorithms. In is planned that the experimental RF data be acquired using the 2D array transducer in the laboratory. A cube phantom made of gelatin will be used, with a square plate put on its top. The external compression can be applied by pressing the plate in the axial direction. The 2D array transducer acquires both the pre- and post-

compression RF signals, which will be processed using the 3D elastography algorithm. Because the 3D technique outperforms the 2D technique in simulation, it can be expected that the 3D technique will provide elastograms with higher image quality using the experimental data than the 2D technique.

REFERENCES

Alam SK and Ophir J. Reduction of signal decorrelation from mechanical compression of tissues by temporal stretching: applications to elastography. Ultrasound in Med. & Biol., 1997; 23: 95-105.

Alam SK, Ophir J and Konofagou EE. An adaptive strain estimator for elastography. IEEE Transactions on Ultrasonics, Ferroelectrics and Frequency Control, 1998; 45: 461-472.

Anderson WAD and Kissane JM. Pathology, 9th ed. St. Louis, Mosby Co., 1953.

Ariel IM and Cleary JB, Breast cancer diagnosis and treatment. New York, McGraw-Hill, 1987.

Basarab A, Liebgott H, Morestin F, Lyshchik A, Higashi T, Asato R and Delachartre P. A method for vector displacement estimation with ultrasound imaging and its application for thyroid nodular disease. Medical Imaging Analysis, 2008; 12: 259-274.

Bilgen M and Insana M. Predicting target detectability in acoustic elastography. IEEE Ultrasonic Symposium, 1997; 2: 1427-1430.

Brusseau E, Perrey C, Delachartre P, Vogt M, Vray D and Ermert H. Axial strain imaging using a local estimation of the scaling factor from RF ultrasound signals. Ultrasound Imaging, 2000; 22: 95-107.

Céspedes I and Ophir J. Reduction of image noise in elastography. Ultrasonic Imaging, 1993; 15: 89-102.

Céspedes I, Ophir J and Alam SK. The combined effect of signal decorrelation and random noise on the variance of time delay estimation. IEEE Transactions on Ultrasonics, Ferroelectrics and Frequency Control, 1997; 44: 220-225.

Chaudhry A. Effect of boundary conditions on performance of poroelastographic imaging techniques in non-homogenous poroelastic media. A Master's Thesis, Texas A&M University, College Station, TX, 2010.

Deprez J-F, Brusseau E and Basset O. 3D strain imaging method adapted to large deformations and freehand scanning. IEEE International Ultrasonics Symposium Proceedings, 2008; 544-547.

Deprez J-F, Brusseau E, Schmitt C, Cloutier G and Basset O. 3D estimation of soft biological tissue deformation from radio-frequency ultrasound volume acquisitions. Medical Image Analysis, 2009; 13: 116-127.

Doyley MM, Bamber JC, Fuechsel F and Bush NL. A freehand elastographic imaging approach for clinical breast imaging: system development and performance evaluation. Ultrasound in Med. & Biol, 2001; 27(10): 1347-1357.

Emelianov SY, Lubinski MA, Weitzel WF, Wiggins RC and Skovoroda AR, et al. Elasticity imaging for early detection of renal pathology. Ultrasound in Med. & Biol, 1995; 21: 871-883.

Garra BS, Céspedes EI, Ophir J, Spratt SR and Zuurbier RA, et al. Elastography of breast lesions: initial clinical results. Radiology, 1997; 202: 79-86.

Gaspari R, Blehar D , Mendoza M, Montoya A, Moon C and Polan D. Use of ultrasound elastography for skin and subcutaneous abscesses. J. Ultrasound Med., 2009; 28: 855-860.

Hall JT, Zhu Y, Spalding CS and Cook LT. In-vivo results of real-time freehand elasticity imaging. IEEE International Symposium on Biomedical Imaging, 2002; 805-808.

Hiltawsky KK, Krüger M, Starke C, Heuser L and Ermert H, et al. Freehand ultrasound elastography of breast lesions: clinical results. Ultrasound in Med. & Biol, 2001; 27(11): 1461-1469.

Kallel F and Ophir J. Three-dimensional tissue motion and its effect on image noise in elastography. IEEE Transactions on Ultrasonics, Ferroelectrics and Frequency Control, 1997; 44: 1286-1296.

Konofagou EE, Harrigan T and Ophir J. Shear strain estimation and lesion mobility assessment in elastography. Ultrasonics, 2000; 38: 400-404.

Konofagou EE and Ophir J. Precision estimation and imaging of normal and shear components of the 3D strain tensor in elastography. Phys. Med. Biol., 2000; 45: 1553-1563.

Konofagou EE , Harrigan T, Ophir J and Krouskop T. Poroelastography: estimating and imaging the poroelastic properties of tissues. IEEE Ultrasonics Symposium, 2001; 27: 1387-1397.

Konofagou EE, D'Hooge J and Ophir J. Myocardial elastography−a feasibility study in vivo. Ultrasound in Med. & Biol, 2002; 28: 475-482.

Lee RT, Grodzynsky AJ, Frank EH, Kamm RD and Schoen FJ. Structure-dependent dynamic mechanical behavior of fibrous caps from human atherosclerotic plaques. Circulation, 1991; 83: 1764-1770.

Lendon CL, Davies MJ, Born GV and Richardson PD. Atherosclerotic plaque caps are locally weakened when macrophage density is increased. Atherosclerosis, 1991; 87: 87-90.

Lindop JE, Treece GM, Gee AH and Prager RW. 3D elastography using freehand ultrasound. Ultrasound in Med. & Biol., 2006; 32: 529-545.

Lorenz A, Sommerfeld HJ, Schürmann MG, Philippou S and Senge T, et al. A new system for the acquisition of ultrasonic multicompression strain images of the human prostate in vivo. IEEE Transactions on Ultrasonics, Ferroelectrics and Frequency Control, 1999; 46(5): 1147-1154.

Lurie AI. Theory of elasticity. Berlin, Heidelberg, New York, Springer, 2005.

Ophir J, Céspedes I, Ponnekanti H, Yazdi Y and Li X. Elastography: a method for

imaging the elasticity of biological tissues. Ultrasound Imaging, 1991; 13: 111-134.

Ophir J, Céspedes I, Garra B, Ponnekanti H and Huang Y, et al. Elastography: Ultrasonic imaging of tissue strain and elastic modulus in vivo. Eur. J. Ultrasound, 1996; 3: 49-70.

Ophir J, Kallel F, Varghese T, Bertrand M and Céspedes I, et al. Elastography: A systems approach. Int. J. Imaging Syst. Technol., 1997; 8: 89-103.

Ophir J, Alam SK, Garra B, Kallel F and Konofagou EE, et al. Elastography: Ultrasonic estimation and imaging of the elastic properties of tissues. Proceedings of the Institute of Mechanical Engineering Part HJ. Eng. Med., 1999; 213: 203-233.

Patil AV, Krouskop TA, Ophir J and Srinivasan S. On the differences between two-dimensional and three-dimensional simulations for assessing elastographic image quality: a simulation study. Ultrasound in Med. & Biol., 2008; 34: 1129-1138.

Phillip LG. Introduction to linear elasticity (2^{nd} edition). New York, Springer-Verlag, 1994.

Po L-M and Ma W-C. A novel four-step search algorithm for fast block motion estimation. IEEE Transactions on Circuits and Systems for Video Technology, 1996; 6: 313-317.

Righetti R, Kallel F, Stafford RJ, Price RE and Krouskop TA, et al. Elastographic

characterization of HIFU-induced lesions in canine livers. Ultrasound in Med. & Biol., 1999; 25: 1099-1113.

Righetti R and Ophir J. Axial resolution in elastography. Ultrasound in Med. & Biol., 2002; 28: 695-704.

Righetti R, Srinivasan S and Ophir J. Lateral resolution in elastography. Ultrasound in Med. & Biol., 2003; 29: 101-113.

Seferidis V and Ghanbari M. Generalised block-matching motion estimation using quad-tree structured spatial decomposition. IEEE Proceedings Vision Image Signal Process, 1994; 141: 446-452.

Srinivasan S, Kallel K, Souchon R and Ophir J. Analysis of an adaptive strain estimation technique in elastography. Ultrasonic Imaging, 2002a; 24:109-118.

Srinivasan S, Ophir J and Alam SK. Elastographic imaging using staggered strain estimates. Ultrasonic Imaging, 2002b; 24: 229-245.

Srinivasan S, Righetti R and Ophir J. Trade-offs between the axial resolution and the signal-to-noise ratio in elastography. Ultrasound in Med. & Biol., 2003; 29: 847-866.

Stavros AT, Thickman D and Rapp CL. Solid breast modules: use of sonography to distinguish between benign and malignant lesions. Radiology, 1995; 196: 123-134.

Thitaikumar Arun, Krouskop TA and Ophir J. Signal-to-noise ratio, contrast-to-noise

ratio and their trade-offs with resolution in axial-shear strain elastography. Phys. Med. Biol., 2007; 52: 13-28.

Varghese T, Ophir J and Céspedes I. Noise reduction in elastograms using temporal stretching with multicompression averaging. Ultrasound in Med. & Biol., 1996; 22: 1043-1052.

Varghese T and Ophir J. Estimating tissue strain from signal decorrelation using the correlation coefficient. Ultrasound in Med. & Biol., 1996; 22: 1249-1254.

Varghese T and Ophir J. A theoretical framework for performance characterization of elastography: the strain filter. IEEE Transactions on Ultrasonics, Ferroelectrics and Frequency Control, 1997; 44: 164-172.

Varghese T, Zagzebski JA and Techavipoo U. Elastographic imaging of thermal lesions in-vivo. In: Linzer M, ed. 27th International Symposium on Ultrasonic Imaging and Tissue Characterization, Arlington, VA. Ultrasonic Imaging, 2002; 22:175.

Yeung F, Levinson SF and Parker KJ. Multilevel and motion model-based ultrasonic speckle tracking algorithms. Ultrasound in Med. & Biol., 1998; 24: 427-441.

APPENDIX

BASIC CONCEPTS

Elastic (Phillip 1994):

A material that is loaded only to a level below the yield strain and that unloads along the same path is called elastic.

Stress (Phillip 1994):

The stress vector represents the force intensity at the point of the particular orientation of area element. The normal stress σ is defined as the average normal force F_n on the area A:

$$\sigma = \frac{F_n}{A}$$

And the shear stress τ is defined as the average transverse force F_s on the area A:

$$\tau = \frac{F_s}{A}$$

Strain:

Strain is a normalized measure of deformation representing the displacement between particles in the material (Phillip 1994).

Normal strain is the relative elongation of the material and shear strain is the change in angle between two originally orthogonal directions in the material.

The strain tensor e_{ij} has a relationship with the displacements (Thitaikumar et al. 2007):

$$\text{Normal strains: } e_x = \frac{\partial u}{\partial x},\ e_y = \frac{\partial v}{\partial y},\ e_z = \frac{\partial w}{\partial z}$$

$$\text{Shear strains: } \quad e_{xy} = \frac{\partial u}{\partial y} + \frac{\partial v}{\partial x}$$

$$e_{yz} = \frac{\partial v}{\partial z} + \frac{\partial w}{\partial y}$$

$$e_{xz} = \frac{\partial w}{\partial x} + \frac{\partial u}{\partial z}$$

where u is the displacement along x direction, v is the displacement along y direction and w is the displacement along z direction.

The shear strains are usually generated at the boundaries between different materials when an external compression in the axial direction is applied (Thitaikumar et al. 2007). The magnitude and distribution of the shear strains are determined by the boundary conditions, the orientation of the interfaces, the elastic modulus of the material and the amount of the compression. It is reported that the shear strain images provide clinically

useful information, such as the differentiating between various types of breast tumors (Konofagou et al. 2000).

Because the lateral resolution of an ultrasonic system is much lower than the axial resolution, the quality of the lateral-shear strain estimate is remarkably poorer than that of the axial-shear strain estimate. Consequently, only the axial-shear strain is estimated and analyzed in this work. Fortunately, in the case of circularly symmetric inclusions, which are chosen in this work, the axial-shear strain alone may provide adequate information (Stavros et al. 1995).

Poisson's ratio (Lurie 2005):

When the material is extended by an axial force, it will expand in transverse directions. Poisson's ratio is the ratio of the transverse contraction strain to the axial extension strain:

$$\nu = -\frac{e_{trans}}{e_{axial}}$$

Young's modulus (Lurie 2005):

Young's modulus is a measure of the stiffness of an isotropic elastic material. It is the ratio of the axial stress over the axial strain:

$$E = \frac{\sigma_{axial}}{e_{axial}}$$

Shear modulus (Lurie 2005):

The shear modulus is the ratio of shear stress over shear strain:

$$G = \frac{\sigma_{shear}}{e_{shear}}$$

VITA

Name:	Mohan Li
Address:	Department of Electrical and Computer Engineering 232-E WERC 3128 TAMU College Station, Texas, 77840-3128
Email Address:	mohanli@neo.tamu.edu
Education:	B.S., Electrical Engineering, University of Science and Technology of China M.S., Electrical Engineering, Texas A&M University